

Directional quasi-analytic wavelet packets for image restoration

Amir Averbuch¹ Pekka Neittaanmäki² Valery Zheludev¹ Moshe Salhov¹ Jonathan Hauser³

¹School of Computer Science, ³School of Electrical Engineering
Tel Aviv University, Israel

²Department of Mathematical Information Technology
University of Jyväskylä, Finland

Abstract

The paper addresses the problems of image denoising and inpainting. To solve both these problems, the directional quasi-analytic wavelet packets (qWPs) and new developments described in the paper are used. The qWPs, which are originated from discrete splines, and the transform schemes are designed in [1]. The obtained results for both problems are quite competitive with the best state-of-the-art algorithms. These results are achieved due to the exceptional properties of qWPs that make them a good fit for image processing applications. These properties are: refined frequency resolution, directionality of waveforms with unlimited number of orientations, (anti-)symmetry of waveforms and windowed oscillating structure of waveforms with a variety of frequencies. The algorithms presented in the paper comprise a number of free parameters that enable to have a flexible adaptation to a processed object that are implemented in a fast way using the fast Fourier transform (FFT). In this paper, the denoising procedure consists of qWP decomposition of the noised (degraded) image, application of adaptive localized soft thresholding of the transform coefficients using the *Bivariate Shrinkage* algorithm (BSA) ([21, 7]) and restoration of the image from the thresholded coefficients from one or several decomposition levels. The inpainting is implemented by an iterative scheme, which, in essence, is the Split Bregman Iteration (SBI) procedure supplied by a BSA-based adaptive variable soft thresholding. The numerical denoising experiments demonstrate that qWP-based algorithm performance is competitive with the performance of the best existing denoising algorithms such as *Block-matching and 3D filtering (BM3D)*, *Directional Tensor Product Complex Tight Framelets (TP-CTF)* and *Digital Affine Shear Filter Transform with 2-Layer Structure (DAS-2)*. Especially, it is true for texture-rich images such as “Barbara” and “Fingerprint” that were corrupted by severe noise. In the inpainting experiments, performance comparison between the qWP-based methods and the state-of-the-art algorithms that are based on *Digital Affine Shear* (DAS-1), DAS-2 and TP-CTF transforms takes place. For inpainting of “Barbara” and “Fingerprint” images, qWP-based methods significantly outperform the mentioned algorithms in PSNR and Structural Similarity Index (SSIM) measurements and by visual perception. In most experiments with relatively smooth images, “Lena” and “Boat”, the qWP-based methods produced the highest SSIM values and demonstrated the best resolution of fine details.

1 Introduction

Since the introduction of complex wavelet transforms by Kingsbury [17, 18], which are implemented by the dual-tree scheme (DT-CW), complex wavelet frames and wavelet packets (WPs) have become a field of active research that appears in multiple applications ([13, 15, 14, 25, 20, 5, 10, 26, 11], to

name a few). The advantages of DT_CWs over the standard real wavelet transforms stem from their approximate shift invariance and from some directionality inherent in tensor-products of DT_CWs.

The directionality of the analysing waveforms is of crucial importance in image processing applications because it provides the opportunity to capture lines, edges and texture details in the images. However, directionality of 2D DT_CWs is limited to only 6 directions. The tight tensor-product complex wavelet frames (TP_CTF_n) with different number of directions, are designed in [10, 11] and some of them, in particular TP_CTF₆ and TP_CTF₆[↓], demonstrate excellent performance for image denoising and inpainting.

Some of disadvantages of the above 2D TP_CTF₆ and TP_CTF₆[↓] frames such as, for example, limited and fixed number of directions (14 directions at each decomposition level) are overcome in [6] (algorithm DAS-2) by the incorporation of the two-layer structure, which is inherent in the TP_CTF₆ and TP_CTF_n[↓] frames, into directional filter banks introduced in [12, 27]. This improves the performance of the DAS-2 compared to the TP_CTF₆ on texture-rich images such as “Barbara” and, especially, “Mandrill”, which is not the case on simpler images such as “Lena”, “Boat” and “Goldhill”.

Another extension of complex wavelets is complex wavelet packets (Co_WPs) in [13, 15, 14]. These Co_WP transforms are implemented by the application of the same filters to high-frequency bands as used in DT_CW transforms. Although the low- and high-frequency bands in DT_CW are approximately analytic, this is not the case for the Co_WPs designed in [13, 15, 14]. In addition, as shown in [5] (Fig. 1), much energy transferred into the negative half-bands of the spectra. Another approach to the design of Co_WPs is described in [5]. It is suggested in [5] that in order to retain an approximate analyticity of the dual-tree WP transforms, the filter banks for the second decomposition of the transforms should be the same for both stems of the tree.

Although the potential advantages of the Co_WP transforms are apparent, so far, to the best of our knowledge, none of the Co_WP schemes in the literature have the desired properties such as perfect frequency separation, Hilbert transform relation between real and imaginary parts of the Co_WPs, orthonormality of shifts of real and imaginary parts of the Co_WPs, unlimited number of directions in the multidimensional case, a variety of free parameters and fast and easy implementation.

A family of Co_WP transforms, which possess all the above properties, is designed in [1]. As a base for the design, the family of discrete-time WPs originated from periodic discrete splines of different orders, which are described in [3] (Chapter 4), is used. The real wavelet packets $\psi_{[m],l}^{2r}$, where m is the decomposition level, $l = 0, \dots, 2^m - 1$ is the index of the related frequency band and $2r$ is the order of the generating discrete spline, are extended to the so-called quasi-analytic WPs (qWPs) by using the periodic discrete-time Hilbert transforms (HTs). The two-dimensional (2D) qWPs are derived by a standard tensor products of 1D qWPs. The number of directions of the 2D qWPs depends on the decomposition level. To be specific, the WPs from level m are oriented in $2(2^{m+1} - 1)$ directions. The waveforms are close to directional cosines with various frequencies modulated by localized low-frequency 2D signals. Both one- and two-dimensional transforms are implemented in a very fast ways by using FFT.

The qWP transforms ([1]), which possess the above-mentioned properties, demonstrate that they are beneficial for denoising and inpainting and these capabilities are shown in the paper.

Denoising: It means restoration of images degraded by zero-mean Gaussian noise. The denoising procedure presented in the paper consists of qWP decomposition of the degraded image down to several levels, adaptive soft thresholding of the transform coefficients using the Bivariate

Shrinkage algorithm (BSA) ([21, 7]) and restoration of the image from the thresholded coefficients from either a single or multiple decomposition levels. The numerical experiments demonstrate that the performance of the qWP-based algorithm is quite competitive with the performance of the best existing denoising algorithms such as the *Block-matching and 3D filtering (BM3D)* ([8], *Directional Tensor Product Complex Tight Framelets (TP-CTF)* ([10, 11, 26]) and *Digital Affine Shear Filter Transform with 2-Layer Structure (DAS-2)* ([6]). Especially it is true for texture-rich images such as “Barbara” and “Fingerprint” corrupted by severe noise.

Inpainting: It means restoration of images degraded by missing of a significant share of pixels and, possibly, by an additional Gaussian noise. The paper introduces two qWP-based iterative methods for dealing with the inpainting problem. The computational scheme in Method1 is close to the **Algorithm I** introduced in [22]. In [22], **Algorithm I** uses TP-CTF₆ filter bank that produces excellent inpainting results that outperform (in a PSNR sense) most state-of-the-art methods (see [22] for comparison of methods). In [6], **Algorithm I** is implemented using the SET-4¹ filter banks. On the cartoon images such as “Lena” and “Boat”, TP-CTF₆ achieves better performance than the rest of the members in SET-4. However, the images with texture such as “Fingerprint” and, especially, “Barbara” are inpainted better by the filter bank DAS-2 with increased directionality compared to TP-CTF₆. **Algorithm I** consists of iterative thresholding of the transform coefficients with decreasing localized thresholds. The threshold levels are determined automatically using BSA. In our Method1, we use the qWP transforms instead of the SET-4 filter banks. Due to multiple orientations (30 at the third level and 62 at the fourth level) and the oscillatory structure of testing waveforms, Method1 outperforms all the SET-4 algorithms on the “Barbara” and “Fingerprint” images in PSNR and Structural Similarity Index (SSIM) sense for both. Although on “Lena” and “Boat” images, at least one of the SET-4 algorithms produces the highest PSNR values, in many experiments with “Lena” and almost all experiments with “Boat”, the SSIM outputs from Method1 exceed those from SET-4.

Method2 couples Method1 with the *split Bregman iteration* (SBI) scheme that uses the so-called *analysis-based* approach ([9, 16]). In essence, it is the SBI algorithm supplied with decreasing localized thresholds determined by the BSA. Practically, in all the experiments Method2 outperforms Method1. In many cases, the outperforming is substantial.

Generally, the main advantage of the qWP-based methods consists of their exceptional ability to capture edges of multiple orientations and, due to the oscillatory structure of waveforms, refined texture details.

The paper is organized as follows: Section 2 briefly outlines the periodic discrete-time WPs originated from discrete splines and corresponding transforms that serve as a basis for the design of qWPs. Section 3 provides brief description of the design and implementation of the qWP transforms. Section 4 extends the design of 1D qWPs to the 2D case. The 2D qWPs are defined via tensor products of 1D qWPs. Section 5 describes the qWP-based denoising scheme and presents the experimental results on the restoration of images degraded by additive noise. The performance of the qWP-based algorithm is compared with the performance of the BM3D, cptTP-CTF₆ ([26]) and DAS-2 algorithms. Section 6 describes the qWP-based Method1 and Method2 for image inpainting

¹ SET-4 means the set of the filter banks DAS-2, DAS-1, TP-CTF₆ and TP-CTF₆[↓].

and presents the experimental results on the restoration of images degraded by missing up to 80% of the pixels with additive noise. The performance of the qWP-based methods is compared with the performance of the algorithms that use the SET-4 filter banks. Section 7 discusses the results.

Notations and abbreviations: $N = 2^j$, $\omega \stackrel{\text{def}}{=} e^{2\pi i/N}$ and $\Pi[N]$ is a space of real-valued N -periodic signals. $\Pi[N, N]$ is the space of two-dimensional N -periodic arrays in both vertical and horizontal directions. The sequence $\delta[k] \in \Pi[N]$ means the N -periodic Kronecker delta.

A signal $\mathbf{x} = \{x[k]\} \in \Pi[N]$ is represented by its inverse discrete Fourier transform (IDFT)

$$\begin{aligned} x[k] &= \frac{1}{N} \sum_{n=0}^{N-1} \hat{x}[n] \omega^{kn} = \frac{1}{N} \sum_{n=-N/2}^{N/2-1} \hat{x}[n] \omega^{kn}, \\ \hat{x}[n] &= \sum_{k=0}^{N-1} x[k] \omega^{-kn}, \quad \hat{x}[-n] = \hat{x}[N-n] = \hat{x}[n]^*, \end{aligned} \quad (1.1)$$

where \cdot^* means complex conjugate. In particular, $\hat{x}[0] = \sum_{k=0}^{N-1} x[k]$ and $\hat{x}[N/2] = \sum_{k=0}^{N-1} (-1)^k x[k]$ are real numbers. The DFT of an N_m -periodic signal is $\hat{x}[n]_m = \sum_{k=0}^{N_m-1} x[k] \omega^{-kn2^m}$.

The abbreviation PR means perfect reconstruction. HT is the Hilbert transform, $H(\mathbf{x})$ is the discrete periodic HT of a signal \mathbf{x} .

The abbreviations WP, cWP and qWP mean wavelet packets (typically spline-based wavelet packets $\psi_{[m],l}^{2r}$), complimentary wavelet packets $\varphi_{[m],l}^{2r}$ and quasi-analytic wavelet packets $\Psi_{\pm[m],l}^{2r}$, respectively, in 1D case, and wavelet packets $\psi_{[m],j,l}^{2r}$, complimentary wavelet packets $\varphi_{[m],j,l}^{2r}$ and quasi-analytic wavelet packets $\Psi_{+\pm[m],l,j}^{2r}$, respectively, in 2D case. The abbreviation WPT means the wavelet packet transform. The abbreviation qWPA designates the image denoising algorithm based on the qWP transforms.

The following N -periodic sequences will be repeatedly used:

$$\beta[n] \stackrel{\text{def}}{=} \frac{\cos^{2r} \frac{\pi n}{N}}{\sqrt{U^{4r}[n]}}, \quad \alpha[n] = \omega^n \beta \left[n + \frac{N}{2} \right] = \omega^n \frac{\sin^{2r} \frac{\pi n}{N}}{\sqrt{U^{4r}[n]}}, \quad (1.2)$$

$$U^{4r}[n] \stackrel{\text{def}}{=} \frac{1}{2} \left(\cos^{4r} \frac{\pi n}{N} + \sin^{4r} \frac{\pi n}{N} \right). \quad (1.3)$$

Peak Signal-to-Noise ratio (PSNR) in decibels (dB) is

$$PSNR \stackrel{\text{def}}{=} 10 \log_{10} \left(\frac{N 255^2}{\sum_{k=1}^N (x_k - \tilde{x}_k)^2} \right) dB. \quad (1.4)$$

SSIM means Structural Similarity Index. BSA stands for Bivariate Shrinkage algorithm and p-filter means periodic filter. SBI stands for split Bregman iteration.

SET-4 means the set of the filter banks DAS-2, DAS-1, TP-CTF₆ and TP-CTF₆[↓].

2 Outline of orthonormal WPs originated from discrete splines: preliminaries

This section provides a brief outline of periodic discrete-time wavelet packets originated from discrete splines and the corresponding transforms. For details see Chapter 4 in [3].

2.1 Periodic discrete spline space and its orthogonal complement

The centered span-two N -periodic discrete B-spline \mathbf{b}^{2r} of order $2r$ is defined as the IDFT of the sequence $\hat{b}^{2r}[n] = \cos^{2r} \frac{\pi n}{N}$. The B-splines are non-negative symmetric finite-length signals (up to periodization). Only the samples $b^{2r}[k]$, $k = -r, \dots, r$, are non-zero.

The signals $s^{2r}[k] \stackrel{\text{def}}{=} \sum_{l=0}^{N/2-1} q[l] b^{2r}[k - 2l]$, which are referred to as discrete splines, form an $N/2$ -dimensional subspace ${}^{2r}\mathcal{S}_{[1]}^0$ of the space $\Pi[N]$ whose basis consists of two-sample shifts of the B-spline \mathbf{b}^{2r} . Here $\mathbf{q} = \{q[l]\}$, $l = 0, \dots, N/2 - 1$, is a real-valued sequence. The DFT of the discrete spline \mathbf{s}^{2r} is $\hat{s}^{2r}[n] = \hat{q}[n]_1 \hat{b}^{2r}[n] = \hat{q}[n]_1 \cos^{2r} \frac{\pi n}{N}$.

The discrete spline $\psi_{[1],0}^{2r} \in {}^{2r}\mathcal{S}_{[1]}^0$ is defined through its IDFT by $\psi_{[1],0}^{2r}[k] \stackrel{\text{def}}{=} \frac{1}{N} \sum_{n=-N/2}^{N/2-1} \omega^{kn} \beta[n]$, where $\beta[n]$ is defined in Eq. (1.2).

The orthogonal complement of the subspace ${}^{2r}\mathcal{S}_{[1]}^0$ in the space $\Pi[N]$ is defined by ${}^{2r}\mathcal{S}_{[1]}^1$. Define the signals $\psi_{[1],1}^{2r}[k] \stackrel{\text{def}}{=} \frac{1}{N} \sum_{n=-N/2}^{N/2-1} \omega^{kn} \alpha[n]$, where $\alpha[n]$ is given in Eq. (1.2).

Proposition 2.1 ([3], Chapter 4) *Two-sample shifts $\{\psi_{[1],\lambda}^{2r}[\cdot - 2l]\}$, $l = 0, \dots, N/2 - 1$, $\lambda = 0, 1$ of the signals $\psi_{[1],\lambda}^{2r}$ form orthonormal bases of the subspaces ${}^{2r}\mathcal{S}_{[1]}^\lambda \subset \Pi[N]$, $\lambda = 0, 1$, respectively.*

The orthogonal projection of a signal $\mathbf{x} \in \Pi[N]$ onto the space ${}^{2r}\mathcal{S}_{[1]}^\lambda$ is the signal $\mathbf{x}_{[1]}^\lambda \in \Pi[N]$ such that

$$\begin{aligned} x_{[1]}^\lambda[k] &= \sum_{l=0}^{N/2-1} y_{[1]}^\lambda[l] \psi_{[1],\lambda}^{2r}[k - 2l], \quad y_{[1]}^\lambda[l] = \langle \mathbf{x}, \psi_{[1],\lambda}^{2r}[\cdot - 2l] \rangle = \sum_{k=0}^{N-1} h_{[1]}^\lambda[k - 2l] x[k], \\ h_{[1]}^\lambda[k] &= \psi_{[1],\lambda}^{2r}[k], \quad \hat{h}_{[1]}^\lambda[n] = \hat{\psi}_{[1],\lambda}^{2r}[n] = \begin{cases} \beta[n], & \text{for } \lambda = 0; \\ \alpha[n], & \text{for } \lambda = 1. \end{cases} \end{aligned} \quad (2.1)$$

Remark 2.1 *We emphasise that the DFTs $\hat{\psi}_{[1],0}^{2r}[N/2] = 0$ and $\hat{\psi}_{[1],1}^{2r}[0] = 0$.*

Definition 2.2 *The signals $\psi_{[1],0}^{2r}$ and $\psi_{[1],1}^{2r}$ are referred to as the discrete-spline wavelet packets (WPs) of order $2r$ from the first decomposition level.*

Figure 2.1 displays the wavelet packets $\psi_{[1],0}^{2r}$ and $\psi_{[1],1}^{2r}$ of different orders and magnitudes of their DFT spectra (which are the p-filters $\mathbf{h}_{[1]}^0$ and $\mathbf{h}_{[1]}^1$ magnitude responses). It is seen that the wavelet packets are well localized in time domain. The spectra are flat and their shapes tend to rectangular when their orders increase.

2.2 One-level wavelet packet transform of a signal

The transform of a signal $\mathbf{x} \in \Pi[N]$ into the pair $\{\mathbf{y}_{[1]}^0, \mathbf{y}_{[1]}^1\}$ of signals from $\Pi[N/2]$ is referred to as the one-level wavelet packet transform (WPT) of the signal \mathbf{x} . According to Proposition 2.1, the transform is implemented by filtering \mathbf{x} with time-reversed half-band low- and high-pass p-filters $\mathbf{h}_{[1]}^0$ and $\mathbf{h}_{[1]}^1$, respectively, which is followed by downsampling. Thus, the p-filters $\mathbf{h}_{[1]}^0$ and $\mathbf{h}_{[1]}^1$ form a critically sampled analysis p-filter bank $\tilde{\mathbf{H}}_{[1]}^1$. Equation (2.1) implies that its modulation matrix is

$$\tilde{\mathbf{M}}[n] = \begin{pmatrix} \hat{h}_{[1]}^0[n] & \hat{h}_{[1]}^0[n + \frac{N}{2}] \\ \hat{h}_{[1]}^1[n] & \hat{h}_{[1]}^1[n + \frac{N}{2}] \end{pmatrix} = \begin{pmatrix} \beta[n] & \beta[n + \frac{N}{2}] \\ \alpha[n] & \alpha[n + \frac{N}{2}] \end{pmatrix} = \begin{pmatrix} \beta[n] & \omega^{-n} \alpha[n] \\ \alpha[n] & -\omega^n \beta[n] \end{pmatrix}, \quad (2.2)$$

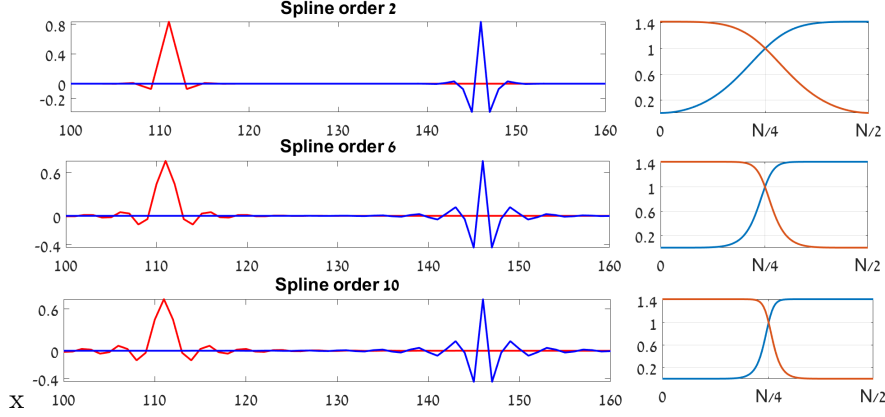


Figure 2.1: Left: WPs $\psi_{[1],0}^{2r}$ (red lines) and $\psi_{[1],1}^{2r}$ (blue lines), $r = 1, 3, 5$. Right: magnitude spectra (positive half-band) of $\psi_{[1],0}^{2r}$ (red lines) and $\psi_{[1],1}^{2r}$ (blue lines)

where $\beta[n]$ and $\alpha[n]$ are defined in Eq. (1.2).

The analysis modulation matrix $\tilde{\mathbf{M}}[n]/\sqrt{2}$, as well as the matrix $\tilde{\mathbf{M}}[-n]/\sqrt{2}$ are unitary matrices. Therefore, the synthesis modulation matrix is

$$\mathbf{M}[n] = \begin{pmatrix} \beta[n] & \alpha[n] \\ \omega^{-n}\alpha[n] & -\omega^n\beta[n] \end{pmatrix} = \tilde{\mathbf{M}}[n]^T. \quad (2.3)$$

Consequently, the synthesis p-filter bank coincides with the analysis p-filter bank and, together, they form a perfect reconstruction (PR) p-filter bank.

The one-level WP transform of a signal \mathbf{x} and its inverse are represented in a matrix form by

$$\begin{pmatrix} \hat{y}_{[1]}^0[n]_1 \\ \hat{y}_{[1]}^1[n]_1 \end{pmatrix} = \frac{1}{2} \tilde{\mathbf{M}}[-n] \cdot \begin{pmatrix} \hat{x}[n] \\ \hat{x}[\vec{n}] \end{pmatrix}, \quad \begin{pmatrix} \hat{x}[n] \\ \hat{x}[\vec{n}] \end{pmatrix} = \mathbf{M}[n] \cdot \begin{pmatrix} \hat{y}_{[1]}^0[n]_1 \\ \hat{y}_{[1]}^1[n]_1 \end{pmatrix} \quad (2.4)$$

where $\vec{n} = n + N/2$.

2.3 Extension of transforms to deeper decomposition levels

Denote by $\tilde{\mathbf{H}}_{[m]} \cup \mathbf{H}_{[m]}$ the PR p-filter bank operating in the space $\Pi[N/2^{m-1}]$ whose modulation matrices are

$$\tilde{\mathbf{M}}_{[m]}[n] = \tilde{\mathbf{M}}[2^{m-1}n], \quad \mathbf{M}_{[m]}[n] = \mathbf{M}[2^{m-1}n], \quad m = 2, \dots, M, \quad (2.5)$$

respectively. The modulation matrices $\tilde{\mathbf{M}}[n]$ and $\mathbf{M}[n]$ are defined in Eqs. (2.2) and (2.3), respectively. The p-filter banks comprise pairs of p-filters $\{\mathbf{h}_{[m]}^0, \mathbf{h}_{[m]}^1\}$ such that their frequency responses are $\hat{h}_{[m]}^\mu[n] = \hat{h}_{[1]}^\mu[2^{m-1}n]$, $\mu = 0, 1$.

Assume that $\lambda = 0, \dots, 2^m - 1$, $\mu = 0, 1$ and denote $\rho = \begin{cases} 2\lambda + \mu, & \text{if } \lambda \text{ is even;} \\ 2\lambda + (1 - \mu), & \text{if } \lambda \text{ is odd.} \end{cases}$

Define iteratively the signals

$$\psi_{[m+1],\rho}^{2r}[n] = \sum_{k=0}^{N/2^m-1} h_{[m+1]}^\mu[k] \psi_{[m],\lambda}^{2r}[n - 2^m k], \quad m = 1, \dots, M. \quad (2.6)$$

Proposition 2.3 ([3]) *The norms of the signals $\psi_{[m+1],\lambda}^{2r} \in \Pi[N]$, $\rho = 0, \dots, 2^{m+1} - 1$, are equal to one. The 2^{m+1} -sample shifts $\left\{ \psi_{[m],\rho}^{2r}[\cdot - 2^{m+1}l] \right\}$, $l = 0, \dots, N/2^{m+1} - 1$, of these signals are mutually orthogonal and signals with different indices ρ are orthogonal to each other.*

Thus, the space $\Pi[N]$ splits into 2^{m+1} mutually orthogonal subspaces $\Pi[N] = \bigoplus_{\rho=0}^{2^{m+1}-1} {}^{2r}\mathcal{S}_{[m+1]}^\rho$ whose orthonormal bases are formed by 2^{m+1} -sample shifts of the signals $\psi_{[m],\rho}^{2r}$, which are referred to as the discrete-spline WPs of order $2r$ from the $m+1$ -th decomposition level.

The orthogonal projection of a signal $\mathbf{x} \in \Pi[N]$ onto the subspace ${}^{2r}\mathcal{S}_{[m+1]}^\rho$ is the signal

$$\begin{aligned} x_{[m+1]}^\rho[k] &= \sum_{l=0}^{N/2^{m+1}-1} y_{[m+1]}^\rho[l] \psi_{[m+1],\rho}^{2r}[k - 2^{m+1}l], \quad k = 0, \dots, N-1, \\ y_{[m+1]}^\rho[l] &= \sum_{l=0}^{N/2^{m+1}-1} \left\langle \mathbf{x}, \psi_{[m+1],\rho}^{2r}[\cdot - 2^{m+1}l] \right\rangle. \end{aligned}$$

The coefficients $y_{[m+1]}^\rho[l]$ are computed iteratively in the frequency domain using the modulation matrices $\tilde{\mathbf{M}}$:

$$\begin{pmatrix} \hat{y}_{[m+1]}^{\rho 0}[n]_{m+1} \\ \hat{y}_{[m+1]}^{\rho 1}[n]_{m+1} \end{pmatrix} = \frac{1}{2} \tilde{\mathbf{M}}[-2^m n] \cdot \begin{pmatrix} \hat{y}_{[m]}^\lambda[n]_m \\ \hat{y}_{[m]}^\lambda[\vec{n}]_m \end{pmatrix}. \quad (2.7)$$

The inverse transform is implemented with the matrices \mathbf{M} :

$$\begin{pmatrix} \hat{y}_{[m]}^\lambda[n]_m \\ \hat{y}_{[m]}^\lambda[\vec{n}]_m \end{pmatrix} = \mathbf{M}[2^m n] \cdot \begin{pmatrix} \hat{y}_{[m+1]}^{\rho 0}[n]_{m+1} \\ \hat{y}_{[m+1]}^{\rho 1}[n]_{m+1} \end{pmatrix}, \quad (2.8)$$

where $\rho 0 = \begin{cases} 2\lambda, & \text{if } \lambda \text{ is even;} \\ 2\lambda + 1, & \text{if } \lambda \text{ is odd,} \end{cases}$ and vice versa for $\rho 1$; $\vec{n} = n + N/2^{m+1}$ and $m = 1, \dots, M$.

Figure 2.2 displays the second-level WPs originating from discrete splines of orders 2, 6 and 10 and their DFTs. One can observe that the wavelet packets are symmetric and well localized in time domain. Their spectra are flat and their shapes tend to rectangular as their orders increase. They split the frequency domain into four quarter-bands.

2.4 2D WPTs

A standard way to extend the 1D WPTs (WPTs) to multiple dimensions is by the tensor-product extension. The 2D one-level WPT of a signal $\mathbf{x} = \{x[k, n]\}$, $k, n = 0, \dots, N-1$, which belongs to $\Pi[N, N]$, consists of the application of 1D WPT to columns of \mathbf{x} , which is followed by the application of the transform to rows of the coefficient array. As a result of the 2D WPT of signals from $\Pi[N, N]$, the space splits into four mutually orthogonal subspaces $\Pi[N, N] = \bigoplus_{j,l=0}^1 {}^{2r}\mathcal{S}_{[1]}^{j,l}$.

The subspace ${}^{2r}\mathcal{S}_{[1]}^{j,l}$ is a linear hull of two-sample shifts of the 2D wavelet packets $\left\{ \psi_{[1],j,l}^{2r}[k - 2p, n - 2t] \right\}$, $p, t = 0, \dots, N/2 - 1$, that form an orthonormal basis of ${}^{2r}\mathcal{S}_{[1]}^{j,l}$. The

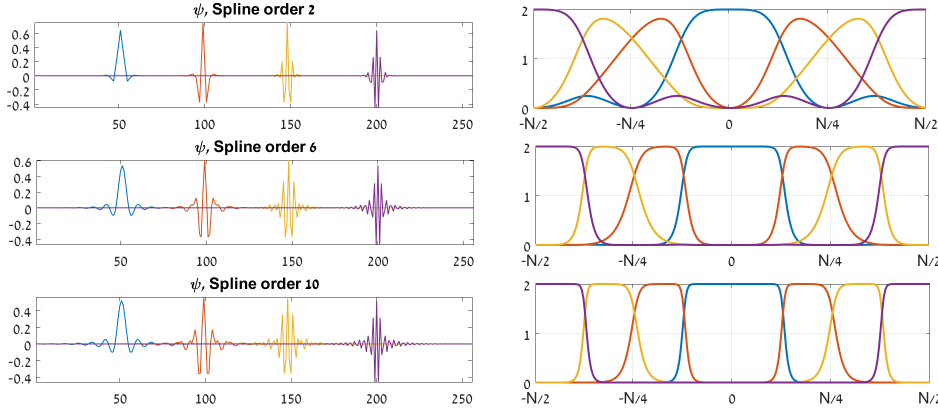


Figure 2.2: Left: second-level discrete-spline WPs of different orders; left to right: $\psi_{[2],0}^{2r} \rightarrow \psi_{[2],1}^{2r} \rightarrow \psi_{[2],2}^{2r} \rightarrow \psi_{[2],3}^{2r}$. Right: magnitude DFT spectra of these wavelet packets

orthogonal projection of a signal $\mathbf{x} \in \Pi[N, N]$ onto the subspace ${}^{2r}\mathcal{S}_{[1]}^{j,l}$ is the signal $\mathbf{x}_{[1]}^{j,l} \in \Pi[N, N]$ such that

$$x_{[1]}^{j,l}[k, n] = \sum_{p,t=0}^{N/2-1} y_{[1]}^{j,l}[p, t] \psi_{[1],j,l}^{2r}[k - 2p, n - 2t], \quad j, l = 0, 1,$$

The 2D wavelet packets are $\psi_{[1],j,l}^{2r}[n, m] \stackrel{\text{def}}{=} \psi_{[1],j}^{2r}[n] \psi_{[1],l}^{2r}[m]$, $j, l = 0, 1$. They are normalized and orthogonal to each other in the space $\Pi[N, N]$. It means that $\sum_{n,m=0}^{N-1} \psi_{[1],j_1,l_1}^{2r}[n, m] \psi_{[1],j_2,l_2}^{2r}[n, m] = \delta[j_1 - j_2] \delta[l_1 - l_2]$. Their two-sample shifts in either direction are mutually orthogonal. The transform coefficients are

$$y_{[1]}^{j,l}[p, t] = \left\langle \mathbf{x}, \psi_{[1],j,l}^{2r}[\cdot - 2p, \cdot - 2t] \right\rangle = \sum_{n,m=0}^{N-1} \psi_{[1],j,l}^{2r}[n - 2p, m - 2t] x[n, m].$$

By the iterated application of the above transforms to blocks of the transform coefficients down to the m -th level, we get that the space $\Pi[N, N]$ is decomposed into 4^m mutually orthogonal subspaces $\Pi[N, N] = \bigoplus_{j,l=0}^{2^m-1} {}^{2r}\mathcal{S}_{[m]}^{j,l}$. The orthogonal projection of the signal $\mathbf{x} \in \Pi[N, N]$ onto the subspace ${}^{2r}\mathcal{S}_{[m]}^{j,l}$ is the signal $\mathbf{x}_{[m]}^{j,l} \in \Pi[N, N]$ such that

$$x_{[m]}^{j,l}[k, l] = \sum_{p,t=0}^{N/2^m-1} y_{[m]}^{j,l}[p, t] \psi_{[m],j,l}^{2r}[k - 2^m p, l - 2^m t], \quad j, l = 0, \dots, 2^m - 1,$$

$$\psi_{[m],j,l}^{2r}[k, n] \stackrel{\text{def}}{=} \psi_{[m],j}^{2r}[k] \psi_{[m],l}^{2r}[n], \quad y_{[m]}^{j,l}[p, t] = \left\langle \mathbf{x}, \psi_{[m],j,l}^{2r}[\cdot - 2^m p, \cdot - 2^m t] \right\rangle.$$

The 2D tensor-product WPs $\psi_{[m],j,l}^{2r}$ are well localized in the spatial domain, their 2D DFT spectra are flat and provide a refined split of the frequency domain of signals from $\Pi[N, N]$.² The drawback is that the WPs are either oriented in horizontal or vertical directions or not at all.

²Especially it is true for WPs derived from higher-order discrete splines.

3 (Quasi-)analytic and complementary WPs

In this section and Section 4, we briefly outline the design and properties of analytic and the so-called quasi-analytic WPs related to the discrete-spline-based WPs discussed in Section 2. For details we refer to [1].

3.1 Analytic periodic signals

Assume that a signal $\mathbf{x} \in \Pi[N]$ is represented by its inverse DFT. Then, Eq. (1.1) can be written as

$$x[k] = \frac{\hat{x}[0] + (-1)^k \hat{x}[N/2]}{N} + \frac{2}{N} \sum_{n=1}^{N/2-1} \frac{\hat{x}[n] \omega^{kn} + (\hat{x}[n] \omega^{kn})^*}{2}.$$

Define the real-valued signal $\mathbf{h} \in \Pi[N]$ and two complex-valued signals $\bar{\mathbf{x}}_+$ and $\bar{\mathbf{x}}_-$ such that

$$h[k] \stackrel{\text{def}}{=} \frac{2}{N} \sum_{n=1}^{N/2-1} \frac{\hat{x}[n] \omega^{kn} - \hat{x}[n]^* \omega^{-kn}}{2i}, \quad (3.1)$$

$$\bar{x}_{\pm}[k] \stackrel{\text{def}}{=} x[k] \pm ih[k] = \frac{\hat{x}[0] + (-1)^k \hat{x}[N/2]}{N} + \frac{2}{N} \sum_{n=1}^{N/2-1} \begin{cases} \hat{x}[n] \omega^{kn}, & \text{for } \bar{x}_+; \\ \hat{x}[n]^* \omega^{-kn}, & \text{for } \bar{x}_-. \end{cases} \quad (3.2)$$

Thus, the signal $\mathbf{h} = H(\mathbf{x})$ can be regarded as the Hilbert transform (HT) of a discrete-time periodic signal \mathbf{x} and the complex-valued signals $\bar{\mathbf{x}}_{\pm}$ are the analytic signals related to \mathbf{x} (see for example [19]).

Proposition 3.1 ([1])

1. If the signal $\mathbf{x} \in \Pi[N]$ is symmetric about a grid point $k = K$ then $\mathbf{h} = H(\mathbf{x})$ is antisymmetric about K and $h[K] = 0$.
2. Assume that a signal $\mathbf{x} \in \Pi[N]$ and $\hat{x}[0] = \hat{x}[N/2] = 0$. Then,
 - (a) The norm of its HT is $\|H(\mathbf{x})\| = \|\mathbf{x}\|$.
 - (b) The magnitude spectra of the signals \mathbf{x} and $\mathbf{h} = H(\mathbf{x})$ coincide.

3.2 Analytic WPs

The analytic spline-based WPs and their DFT spectra are derived from the corresponding WPs $\{\psi_{[m],l}^{2r}\}$, $m = 1, \dots, M$, $l = 0, \dots, 2^m - 1$, in line with the scheme in Section 3.1. Recall that for all $l \neq 0$, the DFT $\hat{\psi}_{[m],l}^{2r}[0] = 0$ and for all $l \neq 2^m - 1$, the DFT $\hat{\psi}_{[m],l}^{2r}[N/2] = 0$.

Denote by $\theta_{[m],l}^{2r} = H(\psi_{[m],l}^{2r})$ the discrete periodic HT of the wavelet packet $\psi_{[m],l}^{2r}$. Then, the corresponding analytic WPs are $\bar{\psi}_{\pm[m],l}^{2r} = \psi_{[m],l}^{2r} \pm i\theta_{[m],l}^{2r}$.

Properties of the analytic WPs

1. The DFT spectra of the analytic WPs $\bar{\psi}_{+[m],l}^{2r}$ and $\bar{\psi}_{-[m],l}^{2r}$ are located within the bands $[0, N/2]$ and $[N/2, N] \iff [-N/2, 0]$, respectively.
2. The real component $\psi_{[m],l}^{2r}$ is the same for both WPs $\bar{\psi}_{\pm[m],l}^{2r}$. It is a symmetric oscillating waveform.
3. The HT WPs $\theta_{[m],l}^{2r} = H(\psi_{[m],l}^{2r})$ are antisymmetric oscillating waveforms.
4. For all $l \neq 0, 2^m - 1$, the norms $\|\theta_{[m],l}^{2r}\| = 1$. Their magnitude spectra $|\hat{\theta}_{[m],l}^{2r}[n]|$ coincide with the magnitude spectra of the respective WPs $\psi_{[m],l}^{2r}$.
5. When either $l = 0$ or $l = 2^m - 1$, the magnitude spectra of $\theta_{[m],l}^{2r}$ coincide with that of $\psi_{[m],l}^{2r}$ everywhere except for the points $n = 0$ or $N/2$, respectively, and the waveforms' norms are no longer equal to 1.

The properties in items 3–5 follow directly from Proposition 3.1.

Proposition 3.2 ([1]) *For all $l \neq 0, 2^m - 1$, the shifts of the HT WPs $\{\theta_{[m],l}^{2r}[\cdot - 2^m l]\}$ are orthogonal to each other in the space $\Pi[N]$. The orthogonality does not take place for $\theta_{[m],0}^{2r}$ and $\theta_{[m],2^m-1}^{2r}$.*

3.3 Complementary set of wavelet packets and quasi-analytic WPs

3.3.1 Complementary orthonormal WPs

The discrete-spline-based WPs $\{\psi_{[m],l}^{2r}\}$ are normalized and their 2^m -sample shifts are mutually orthogonal. Combinations of shifts of several wavelet packets can form orthonormal bases for the signal space $\Pi[N]$. On the other hand, it is not true for the set $\{\theta_{[m],l}^{2r}\}$, $l = 0, \dots, 2^m - 1$, of the antisymmetric waveforms, which are the HTs of the WPs $\{\psi_{[m],l}^{2r}\}$. At the decomposition level m , the waveforms $\{\theta_{[m],l}^{2r}\}$, $l = 1, \dots, 2^m - 2$, are normalized and their 2^m -sample shifts are mutually orthogonal, but the norms of the waveforms $\theta_{[m],0}^{2r}$ and $\theta_{[m],2^m-1}^{2r}$ are close but not equal to 1 and their shifts are not mutually orthogonal. It happens because the values $\hat{\theta}_{[m],j}^{2r}[0]$ and $\hat{\theta}_{[m],j}^{2r}[N/2]$ are missing in their DFT spectra. Keeping this in mind, we upgrade the set $\{\theta_{[m],l}^{2r}\}$, $l = 0, \dots, 2^m - 1$ in the following way.

Define a set $\{\varphi_{[m],l}^{2r}\}$, $m = 1, \dots, M$, $l = 0, \dots, 2^m - 1$, of signals from the space $\Pi[N]$

$$\varphi_{[m],l}^{2r}[k] \stackrel{\text{def}}{=} \hat{\psi}_{[m],l}^{2r}[0]/N + \hat{\psi}_{[m],l}^{2r}[N/2]/N + \theta_{[m],l}^{2r}[k]. \quad (3.3)$$

For all $l \neq 0, 2^m - 1$, the signals $\varphi_{[m],l}^{2r}$ coincide with $\theta_{[m],l}^{2r} = H(\psi_{[m],l}^{2r})$ ³.

Proposition 3.3

³Recall that the values $\hat{\psi}_{[m],l}^{2r}[0]/N$ and $\hat{\psi}_{[m],l}^{2r}[N/2]/N$ are real.

- The magnitude spectra $|\hat{\varphi}_{[m],l}^{2r}[n]|$ coincide with the magnitude spectra of the respective WPs $\psi_{[m],l}^{2r}$.
- For any $m = 1, \dots, M$, and $l = 1, \dots, 2^m - 2$, the signals $\varphi_{[m],l}^{2r}$ are antisymmetric oscillating waveforms. For $l = 0$ and $l = 2^m - 1$, the shapes of the signals are near antisymmetric.
- The orthonormality properties, which are similar to the properties of WPs $\psi_{[m],l}^{2r}$, hold for the signals $\varphi_{[m],l}^{2r}$ such that $\langle \varphi_{[m],l}^{2r}[\cdot - p 2^m], \varphi_{[m],\lambda}^{2r}[\cdot - s 2^m] \rangle = \delta[\lambda, l] \delta[p, s]$.

We call the signals $\{\varphi_{[m],l}^{2r}\}$, $m = 1, \dots, M$, $l = 0, \dots, 2^m - 1$, the *complementary wavelet packets* (cWPs). Similarly to the WPs $\{\psi_{[m],l}^{2r}\}$, combinations of the cWPs can provide a variety of orthonormal bases for the space $\Pi[N]$.

3.3.2 Quasi-analytic WPs

The sets of complex-valued WPs, which we refer to as the quasi-analytic wavelet packets (qWP), are defined as $\Psi_{\pm[m],l}^{2r} = \psi_{[m],l}^{2r} \pm i\varphi_{[m],l}^{2r}$, $m = 1, \dots, M$, $l = 0, \dots, 2^m - 1$, where $\varphi_{[m],l}^{2r}$ are the cWPs defined in Eq. (3.3). The qWPs $\Psi_{\pm[m],l}^{2r}$ differ from the analytic WPs $\tilde{\psi}_{\pm[m],l}^{2r}$ by adding the two values $\pm i\hat{\psi}_{[m],l}^{2r}[0]$ and $\pm i\hat{\psi}_{[m],l}^{2r}[N/2]$ into their DFT spectra, respectively. For a given decomposition level m , these values are zero for all l except for $l_0 = 0$ and $l_m = 2^m - 1$. It means that for all l except for l_0 and l_m , the qWPs $\Psi_{\pm[m],l}^{2r}$ are analytic. The DFTs of qWPs are

$$\begin{aligned}\hat{\Psi}_{+[m],l}^{2r}[n] &= \begin{cases} (1+i)\hat{\psi}_{[m],l}^{2r}[n], & \text{if } n = 0 \text{ or } n = N/2; \\ 2\hat{\psi}_{[m],l}^{2r}[n], & \text{if } 0 < n < N/2; \\ 0 & \text{if } -N/2 < n < 0, \end{cases} \\ \hat{\Psi}_{-[m],l}^{2r}[n] &= \begin{cases} (1-i)\hat{\psi}_{[m],l}^{2r}[n], & \text{if } n = 0 \text{ or } n = N/2; \\ 0 & \text{if } 0 < n < N/2; \\ 2\hat{\psi}_{[m],l}^{2r}[n], & \text{if } -N/2 < n < 0. \end{cases}\end{aligned}\quad (3.4)$$

Recall that the real $m+1$ -level WPs $\psi_{[m+1],\rho}^{2r}$ are derived by filtering the m -level WPs $\psi_{[m],\lambda}^{2r}$ with the p-filter $\mathbf{h}_{[m+1]}^\mu$ such that $\hat{h}_{[m]}^{\mu+1}[n] = \hat{h}_{[1]}^\mu[2^m n]$ (see Eq. (2.6)). It turns out that the qWPs are derived iteratively by the same scheme and *with the same filters*.

Proposition 3.4 ([1]) Assume that for a WP $\psi_{[m+1],\rho}^{2r}$, $m = 1, \dots, M$, the relation in Eq. (2.6) holds. Then, for the qWPs $\Psi_{\pm[m+1],\rho}^{2r}$ we have

$$\Psi_{\pm[m+1],\rho}^{2r}[n] = \sum_{k=0}^{N/2^m-1} h_{[m+1]}^\mu[k] \Psi_{\pm[m],\lambda}^{2r}[n - 2^m k] \iff \hat{\Psi}_{\pm[m+1],\rho}^{2r}[\nu] = \hat{h}_{[1]}^\mu[2^m \nu]_m \hat{\Psi}_{\pm[m],\lambda}^{2r}[\nu]. \quad (3.5)$$

Figure 3.1 displays the WPs $\psi_{[3],l}^6 = \Re(\Psi_{\pm[3],l}^6)$, cWPs $\varphi_{[3],l}^{2r} = \Im(\Psi_{\pm[3],l}^6)$, $l = 0, \dots, 7$ from the third decomposition level, and their magnitude spectra that coincide with each other. These (c)WPs provide a collection of diverse symmetric and antisymmetric well localized waveforms, which range from smooth wavelets for $l = 0, 1$ to fast oscillating transients for $l = 5, 6, 7$. Thus, this collection is well suited to catching smooth as well as oscillating patterns in signals. In the 2D case to be

discussed in Section 4, these valuable properties of the spline-based wavelet packets are completed by the directionality of the tensor-product waveforms.

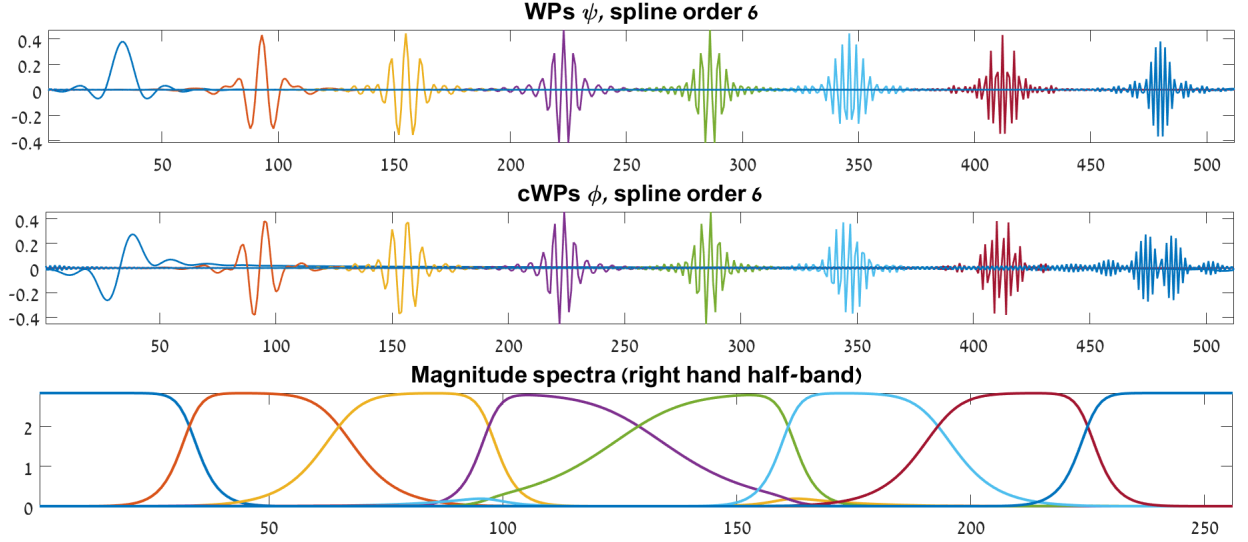


Figure 3.1: Top left to right: third-level WPs $\psi_{[3],l}^{(6)}$, $l = 0, 1, 2, 3, 4, 5, 6, 7$. Center left to right: third-level cWPs $\varphi_{[3],l}^{(6)}$, $l = 0, 1, 2, 3, 4, 5, 6, 7$. Bottom: their magnitude of DFT spectra, respectively, (right hand half-band)

3.4 Implementation of qWP transforms

In this section, we briefly outline the implementation scheme, which is described in details in [1].

3.4.1 One-level transforms

Define the p-filters

$$\mathbf{q}_{\pm[1]}^l \stackrel{\text{def}}{=} \left\{ q_{\pm[1]}^l[k] \right\}, \quad q_{\pm[1]}^l[k] = \psi_{[1],l}^{2r}[k] \pm i \varphi_{[1],l}^{2r}[k] = \Psi_{\pm[1],l}^{2r}, \quad l = 0, 1.$$

Equation (3.4) implies that their frequency responses are

$$\begin{aligned} \hat{q}_{+[1]}^0[n] &= \begin{cases} (1+i)\sqrt{2}, & \text{if } n = 0; \\ 2\beta[n], & \text{if } 0 < n < N/2; \\ 0, & \text{if } N/2 \leq n < N, \end{cases} & \hat{q}_{+[1]}^1[n] &= \begin{cases} -(1+i)\sqrt{2}, & \text{if } n = N/2; \\ 2\alpha[n], & \text{if } 0 < n < N/2; \\ 0, & \text{if } N/2 < n \leq N. \end{cases} \\ \hat{q}_{-[1]}^0[n] &= \begin{cases} (1-i)\sqrt{2}, & \text{if } n = 0; \\ 2\beta[n], & \text{if } N/2 < n < N, \\ 0, & \text{if } 0 < n \leq N/2; \end{cases} & \hat{q}_{-[1]}^1[n] &= \begin{cases} -(1-i)\sqrt{2}, & \text{if } n = N/2; \\ 2\alpha[n], & \text{if } N/2 < n \leq N; \\ 0, & \text{if } 0 \leq n < N/2, \end{cases} \end{aligned}$$

where $\beta[n]$ and $\alpha[n]$ are given in Eq. (1.2). Thus, the analysis modulation matrices for the p-filters $\mathbf{q}_{\pm[1]}^l$ are

$$\tilde{\mathbf{M}}_+^q[n] = \begin{pmatrix} \hat{q}_{+[1]}^0[n] & 0 \\ \hat{q}_{+[1]}^1[n] & -\sqrt{2}(1+i)\delta[n-N/2] \end{pmatrix}, \quad (3.6)$$

$$\tilde{\mathbf{M}}_-^q[n] = \begin{pmatrix} (1-i)\sqrt{2}\delta[n] & \hat{q}_{-[1]}^0[n] \\ 0 & \hat{q}_{-[1]}^1[n] \end{pmatrix}, \quad (3.7)$$

where the modulation matrix $\tilde{\mathbf{M}}[n]$ is defined in Eq. (2.2). Application of the matrices $\tilde{\mathbf{M}}_{\pm}^q[n]$ to the vector $(\hat{x}[n], \hat{x}[\vec{n}])^T$ produces the vectors

$$\begin{pmatrix} \hat{z}_{\pm[1]}^0[n]_1 \\ \hat{z}_{\pm[1]}^1[n]_1 \end{pmatrix} = \frac{1}{2}(\tilde{\mathbf{M}}_{\pm}^q[n])^* \cdot \begin{pmatrix} \hat{x}[n] \\ \hat{x}[\vec{n}] \end{pmatrix} = \begin{pmatrix} \hat{y}_{[1]}^0[n]_1 \\ \hat{y}_{[1]}^1[n]_1 \end{pmatrix} \mp i \begin{pmatrix} \hat{c}_{[1]}^0[n]_1 \\ \hat{c}_{[1]}^1[n]_1 \end{pmatrix},$$

where

$$y_{[1]}^{\lambda}[l] = \langle \mathbf{x}, \psi_{[1],\lambda}^{2r}[\cdot - 2l] \rangle, \quad c_{[1]}^{\lambda}[l] = \langle \mathbf{x}, \varphi_{[1],\lambda}^{2r}[\cdot - 2l] \rangle.$$

Define the matrices $\mathbf{M}_{\pm}^q[n] \stackrel{\text{def}}{=} \tilde{\mathbf{M}}_{\pm}^q[n]$. The matrices $\tilde{\mathbf{M}}^q[n]$ and $\mathbf{M}^q[n]$ are called the analysis and synthesis modulation matrices for the qWP transform, respectively.

Proposition 3.5 ([1]) *Successive application of filter banks defined by the analysis and synthesis modulation matrices $\tilde{\mathbf{M}}_{\pm}^q[n]$ and $\mathbf{M}_{\pm}^q[n]$ to a signal $\mathbf{x} \in \Pi[N]$ produces the analytic signal $\bar{\mathbf{x}}_{\pm}$ associated with \mathbf{x} .*

3.4.2 Multi-level transforms

It was established in Proposition 3.4 that the qWPs $\Psi_{\pm[m+1],\rho}^{2r}$ from the $m+1$ decomposition level are derived from the m -level qWPs $\Psi_{\pm[m],\lambda}^{2r}$ by filtering with the same p-filters \mathbf{h}^{μ} that are used for the design of real WPs $\psi_{[m+1],\rho}^{2r}$. A similar situation takes place for the derivation of the transform coefficients $\{z_{\pm[m+1]}^{\rho}\}$ from the m -level coefficients $\{z_{\pm[m]}^{\rho}\}$.

Proposition 3.6 ([1]) *The DFTs of the qWP transform coefficients from the $m+1$ -th and m -th decomposition levels are linked as follows:*

$$\begin{pmatrix} \hat{z}_{\pm[m+1]}^{\rho 0}[n]_{m+1} \\ \hat{z}_{\pm[m+1]}^{\rho 1}[n]_{m+1} \end{pmatrix} = \frac{1}{2}\tilde{\mathbf{M}}[-2^m n] \cdot \begin{pmatrix} \hat{z}_{\pm[m]}^{\lambda}[n]_m \\ \hat{z}_{\pm[m]}^{\lambda}[\vec{n}]_m \end{pmatrix}, \quad \begin{pmatrix} \hat{z}_{\pm[m]}^{\lambda}[n]_m \\ \hat{z}_{\pm[m]}^{\lambda}[\vec{n}]_m \end{pmatrix} = \mathbf{M}[2^m n] \cdot \begin{pmatrix} \hat{z}_{\pm[m+1]}^{\rho 0}[n]_{m+1} \\ \hat{z}_{\pm[m+1]}^{\rho 1}[n]_{m+1} \end{pmatrix},$$

where $\rho 0 = \begin{cases} 2\lambda, & \text{if } \lambda \text{ is even;} \\ 2\lambda + 1, & \text{if } \lambda \text{ is odd,} \end{cases}$ and vice versa for $\rho 1$, $\vec{n} = n + N/2^{m+1}$ and $m = 1, \dots, M$.

The modulation matrices $\tilde{\mathbf{M}}[n]$ and $\mathbf{M}[n]$ are defined in Eqs. (2.2) and (2.3), respectively. By the application of the inverse DFT to the arrays $\{\hat{z}_{\pm[m+1]}^{\rho}[n]_{m+1}\}$, we get the arrays

$\{z_{\pm[m+1]}^{\rho}[k] = y_{[m+1]}^{\rho}[k] \pm i c_{[m+1]}^{\rho}[k]\}$ of the transform coefficients with the qWPs $\Psi_{\pm[m+1],\rho}^{2r}$, where

$$y_{[m+1]}^{\rho}[k] = \langle \mathbf{x}, \psi_{[m+1],\rho}^{2r}[\cdot - 2^{m+1}k] \rangle, \quad c_{[m+1]}^{\rho}[k] = \langle \mathbf{x}, \varphi_{[m+1],\rho}^{2r}[\cdot - 2^{m+1}k] \rangle.$$

The transforms are executed in the spectral domain using FFT.

4 Two-dimensional complex wavelet packets

A standard design scheme for 2D wavelet packets is outlined in Section 2.4. The 2D wavelet packets are defined as the tensor products of 1D WPs such that $\psi_{[m],j,l}^{2r}[k,n] = \psi_{[m],j}^{2r}[k] \psi_{[m],l}^{2r}[n]$. The 2^m -sample shifts of the WPs $\{\psi_{[m],j,l}^{2r}\}$, $j, l = 0, \dots, 2^m - 1$, in both directions form an orthonormal basis for the space $\Pi[N, N]$ of arrays that are N -periodic in both directions. The DFT spectrum of such a WP is concentrated in four symmetric spots in the frequency domain.

Similar properties are inherent to the 2D cWPs such that $\varphi_{[m],j,l}^{2r}[k,n] = \varphi_{[m],j}^{2r}[k] \varphi_{[m],l}^{2r}[n]$.

4.1 2D complex WPs and their spectra

The WPs $\{\psi_{[m],j,l}^{2r}\}$ as well as the cWPs $\{\varphi_{[m],j,l}^{2r}\}$ lack the directionality property which is needed in many applications that process 2D data. However, real-valued 2D wavelet packets oriented in multiple directions can be derived from tensor products of complex quasi-analytic qWPs $\Psi_{\pm[m],\rho}^{2r}$.

The complex 2D qWPs are defined as follows:

$$\begin{aligned}\Psi_{++[m],j,l}^{2r}[k,n] &\stackrel{\text{def}}{=} \Psi_{+[m],j}^{2r}[k] \Psi_{+[m],l}^{2r}[n], \\ \Psi_{+-[m],j,l}^{2r}[k,n] &\stackrel{\text{def}}{=} \Psi_{+[m],j}^{2r}[k] \Psi_{-[m],l}^{2r}[n],\end{aligned}$$

where $m = 1, \dots, M$, $j, l = 0, \dots, 2^m - 1$, and $k, n = -N/2, \dots, N/2 - 1$. The real parts of these 2D qWPs are

$$\begin{aligned}\vartheta_{+[m],j,l}^{2r}[k,n] &\stackrel{\text{def}}{=} \Re(\Psi_{++[m],j,l}^{2r}[k,n]) = \psi_{[m],j,l}^{2r}[k,n] - \varphi_{[m],j,l}^{2r}[k,n], \\ \vartheta_{-[m],j,l}^{2r}[k,n] &\stackrel{\text{def}}{=} \Re(\Psi_{+-[m],j,l}^{2r}[k,n]) = \psi_{[m],j,l}^{2r}[k,n] + \varphi_{[m],j,l}^{2r}[k,n],\end{aligned}\tag{4.1}$$

The DFT spectra of the 2D qWPs $\Psi_{++[m],j,l}^{2r}$, $j, l = 0, \dots, 2^m - 1$, are the tensor products of the one-sided spectra of the qWPs $\hat{\Psi}_{++[m],j,l}^{2r}[p,q] = \hat{\Psi}_{+[m],j}^{2r}[p] \hat{\Psi}_{+[m],l}^{2r}[q]$ and, as such, they fill the quadrant $\mathbf{Q}_0 : \{k, n = 0, \dots, N/2 - 1\}$ of the frequency domain, while the spectra of $\Psi_{+-[m],j,l}^{2r}$, $j, l = 0, \dots, 2^m - 1$, fill the quadrant $\mathbf{Q}_1 : \{k = 0, \dots, N/2 - 1, n = -N/2, \dots, -1\}$. Figure 4.1 displays magnitude spectra of the tenth-order 2D qWPs $\Psi_{++[2],j,l}^{10}$ and $\Psi_{+-[2],j,l}^{10}$ from the second decomposition level.

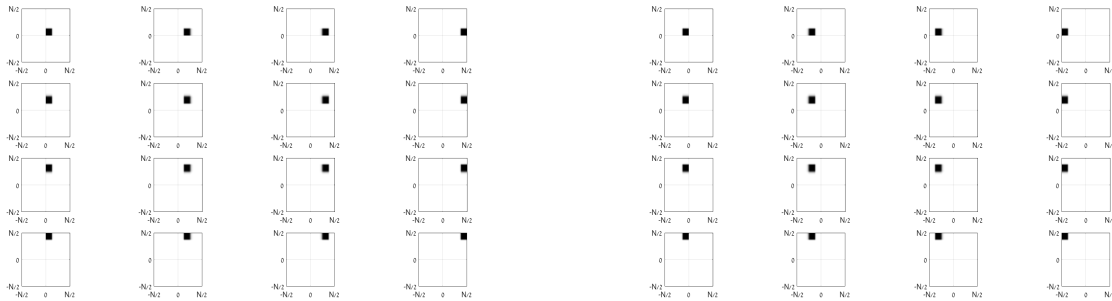


Figure 4.1: Magnitude spectra of 2D qWPs $\Psi_{++[2],j,l}^{10}$ (left) and $\Psi_{+-[2],j,l}^{10}$ (right) from the second decomposition level

Figure 4.1 shows that the DFT spectra of the qWPs $\Psi_{\pm[m],j,l}^{10}$ effectively occupy relatively small squares in the frequency domain. For deeper decomposition levels, sizes of the corresponding squares decrease as geometric progression. Such configuration of the spectra leads to the directionality of the real-valued 2D WPs $\vartheta_{\pm[m],j,l}^{2r}$. The directionality of the WPs $\vartheta_{\pm[m],j,l}^{2r}$ is discussed in [1]. It was shown that if the spectrum of a WP $\Psi_{\pm[m],j,l}^{2r}$ occupies a square whose center lies in the point $[\kappa_0, \nu_0]$, then the respective real-valued WP $\vartheta_{\pm[m],j,l}^{2r}$ is represented by

$$\vartheta_{\pm[m],j,l}^{2r}[k, n] \approx \cos \frac{2\pi(\kappa_0 k + \nu_0 n)}{N} \underline{\vartheta}[k, n],$$

where $\underline{\vartheta}[k, n]$ is a spatially localized waveform. The spectrum of the 2D signal $\underline{\vartheta}$ comprises only low frequencies in both directions and the signal $\underline{\vartheta}$ does not have a directionality. But the 2D signal $\cos \frac{2\pi(\kappa_0 k + \nu_0 n)}{N}$ is oscillating in the direction of the vector $\vec{V} = \kappa_0 \vec{i} + \nu_0 \vec{j}$. Therefore, WP $\vartheta_{\pm[m],j,l}^{2r}$ can be regarded as the directional cosine modulated by the localized low-frequency signal $\underline{\vartheta}$. The cosine frequencies in the vertical and horizontal directions are determined by the indices j and l , respectively, of the WP $\vartheta_{\pm[m],j,l}^{2r}$. The bigger is the index, the higher is frequency in the respective direction. The situation is illustrated in Fig. 4.2.

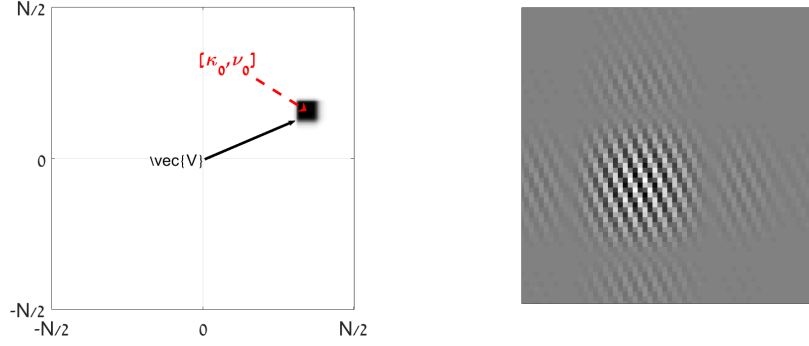


Figure 4.2: Left: magnitude spectra of 2D qWP $\Psi_{++[3],2,5}^{2r}[k, n]$. Right WP $\vartheta_{++[3],2,5}^{2r} = \Re(\Psi_{++[3],2,5}^{2r})$

Figures 4.3 and 4.4 display WPs $\vartheta_{+[2],j,l}^{10}$ and $\vartheta_{-[2],j,l}^{10}$, $j, l = 0, 1, 2, 3$, from the second decomposition level, respectively, and their magnitude spectra

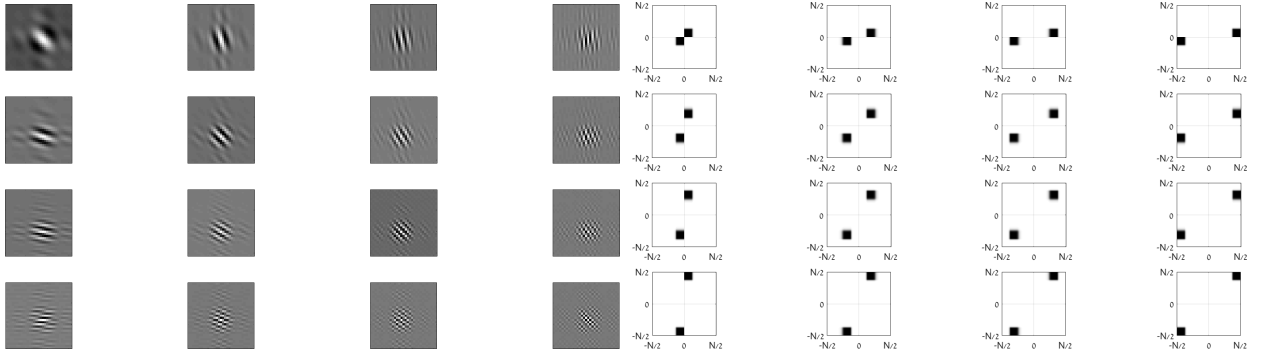


Figure 4.3: WPs $\vartheta_{+[2],j,l}^{10}$ from the second decomposition level (left) and their magnitude spectra (right)

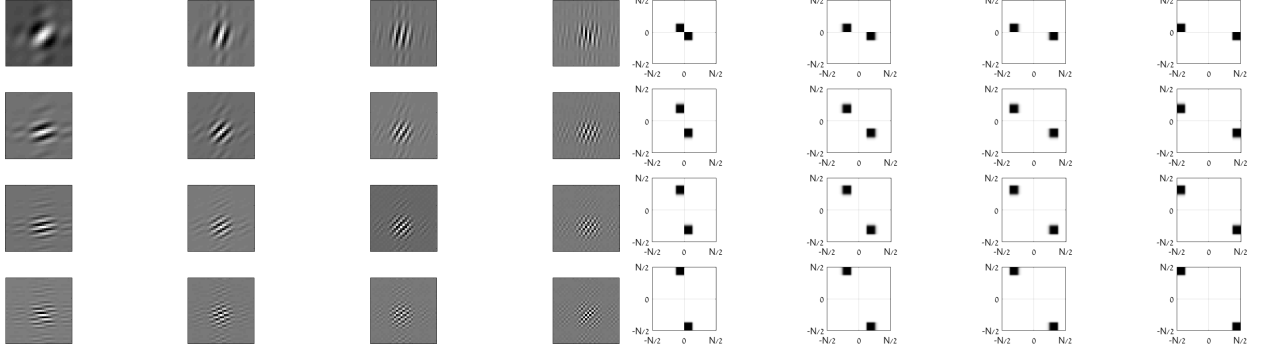


Figure 4.4: WPs $\vartheta_{-[2],j,l}^{10}$ from the second decomposition level (left) and their magnitude spectra (right)

Remark 4.1 Note that orientations of the vectors $\vec{V}_{++[m],j,l}$ and $\vec{V}_{++[m],j+1,l+1}$ are approximately the same. These vectors determine the orientations of the WPs $\vartheta_{+[m],j,l}^{2r}$ and $\vartheta_{+[m],j+1,l+1}^{2r}$, respectively. Thus, these WPs have approximately the same orientation. Consequently, the WPs from the m -th decomposition level are oriented in $2^{m+1} - 1$ different directions. The same is true for the WPs $\vartheta_{-[m],j,l}^{2r}$. Thus, altogether, at level m , we have WPs oriented in $2(2^{m+1} - 1)$ different directions. It is seen in Figs. 4.3, 4.4 and 4.5 that display the WPs $\vartheta_{\pm[3],j,l}^{2r}$.

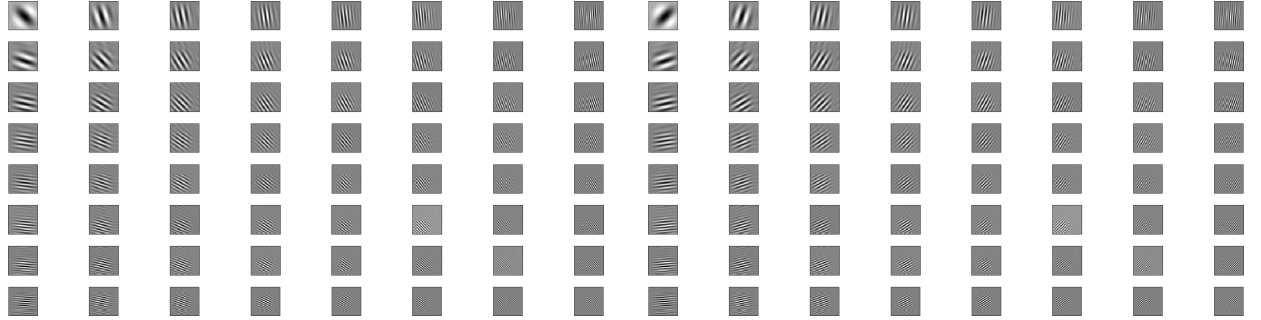


Figure 4.5: WPs $\vartheta_{+[3],j,l}^{10}$ (left 8 columns) and $\vartheta_{-[3],j,l}^{10}$ (right 8 columns) from the third decomposition level

4.2 Outline of the implementation scheme for 2D qWP transforms

The implementation scheme is described in detail in [1]. The spectra of 1D qWPs $\{\Psi_{+[m],j}^{2r}\}$, $j = 0, \dots, 2^m - 1$, fill the non-negative half-band $[0, N/2]$ and vice versa for the qWPs $\{\Psi_{-[m],j}^{2r}\}$, $j = 0, \dots, 2^m - 1$. Therefore, the spectra of 2D qWPs $\{\Psi_{++[m],j,l}^{2r}\}$, $j, l = 0, \dots, 2^m - 1$ fill the quadrant \mathbf{Q}_0 of the frequency domain, while the spectra of 2D qWPs $\{\Psi_{+-[m],j,l}^{2r}\}$ fill the quadrant \mathbf{Q}_1 . It is clearly seen in Fig. 4.6.

Consequently, the spectra of the real-valued 2D WPs $\{\vartheta_{+[m],j,l}^{2r}\}$, $j, l = 0, \dots, 2^m - 1$, and $\{\vartheta_{-[m],j,l}^{2r}\}$ fill the pairs of quadrant $\mathbf{Q}_+ = \mathbf{Q}_0 \cup \mathbf{Q}_2$ and $\mathbf{Q}_- = \mathbf{Q}_1 \cup \mathbf{Q}_3$, respectively.

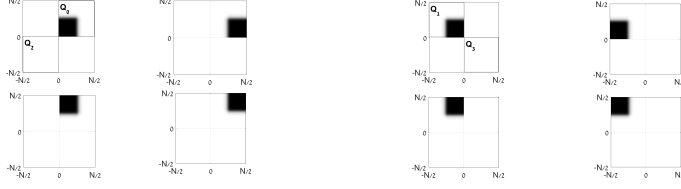


Figure 4.6: Magnitude spectra of WPs $\Psi_{++[1],j,l}^{10}$ (left) and $\Psi_{+-[1],j,l}^{10}$ (right) from the first decomposition level

By this reason, none linear combination of the WPs $\{\vartheta_{+[m],j,l}^{2r}\}$ and their shifts can serve as a basis in the signal space $\Pi[N, N]$. The same is true for WPs $\{\vartheta_{-[m],j,l}^{2r}\}$. However, combinations of the WPs $\{\vartheta_{\pm[m],j,l}^{2r}\}$ provide frames of the space $\Pi[N, N]$.

4.2.1 One-level 2D transforms

The one-level 2D qWP transforms of a signal $\mathbf{X} = \{X[k, n]\} \in \Pi[N, N]$ are implemented by a tensor-product scheme described in Section 2.4. The following outlines the one-level transforms:

Direct transform with $\Psi_{++[1]}^{2r}$: The 1D transform of columns from the signal \mathbf{X} using the modulation matrix $\tilde{\mathbf{M}}_+^q$ defined in Eq. (3.6), which is followed by the 1D transform of rows of the produced coefficient arrays using the same modulation matrix $\tilde{\mathbf{M}}_+^q$, results in the four-blocks transform coefficient array $\mathbf{Z}_{+[1]} = \bigcup_{j,l=0}^1 \mathbf{Z}_{+[1]}^{j,l}$, where

$$Z_{+[1]}^{j,l}[k, n] = \sum_{\lambda, \mu=0}^{N-1} X[\lambda, \mu] \Psi_{++[1],j,l}^{2r}[\lambda - 2k, \mu - 2n], \quad j, l = 0, 1.$$

Direct transform with $\Psi_{+-[1]}^{2r}$: The 1D transform of columns from the signal \mathbf{X} using the modulation matrix $\tilde{\mathbf{M}}_+^q$, which is followed by the 1D transform of rows of the produced coefficient arrays using the same modulation matrix $\tilde{\mathbf{M}}_-^q$ defined in Eq. (3.7), results in the four-blocks transform coefficient array $\mathbf{Z}_{-[1]} = \bigcup_{j,l=0}^1 \mathbf{Z}_{-[1]}^{j,l}$, where

$$Z_{-[1]}^{j,l}[k, n] = \sum_{\lambda, \mu=0}^{N-1} X[\lambda, \mu] \Psi_{+-[1],j,l}^{2r}[\lambda - 2k, \mu - 2n], \quad j, l = 0, 1.$$

Inverse transform with $\Psi_{++[1]}^{2r}$: The 1D inverse transform of rows of the coefficient arrays $\mathbf{Z}_{+[1]}$ using the modulation matrix $\mathbf{M}_+^q = \tilde{\mathbf{M}}_+^q$, which is followed by the 1D inverse transform of columns of the produced coefficient arrays using the same modulation matrix \mathbf{M}_+^q , results in the complex array

$$\mathbf{X}_+ = 4(\mathbf{X} + iH(\mathbf{X}) + i\mathbf{G} - H(\mathbf{G})),$$

where $H(\mathbf{X})$ is the tensor product of the Hilbert transforms of columns and rows of the signal \mathbf{X} and \mathbf{G} is an auxiliary array (see [1]).

Inverse transform with $\Psi_{+-[1]}^{2r}$: The 1D inverse transform of rows of the coefficient arrays $\mathbf{Z}_{-[1]}$ using the modulation matrix $\mathbf{M}_-^q = \tilde{\mathbf{M}}_-^q$, which is followed by the 1D inverse transform of

columns of the produced coefficient arrays using the modulation matrix \mathbf{M}_+^q , results in the complex array

$$\mathbf{X}_- = 4(\mathbf{X} - iH(\mathbf{X}) + i\mathbf{G} + H(\mathbf{G})).$$

Finally, we have the signal \mathbf{X} restored by $\tilde{\mathbf{X}} = \Re(\mathbf{X}_+ + \mathbf{X}_-)/8$.

Figure 4.7 illustrates the image “Barbara” restoration by the 2D signals $\Re(\mathbf{X}_\pm)$. The signal $\Re(\mathbf{X}_+)$ captures edges oriented through *north-east*, while $\Re(\mathbf{X}_-)$ captures edges oriented to *north-west*. The signal $\tilde{\mathbf{X}} = \Re(\mathbf{X}_+ + \mathbf{X}_-)/8$ perfectly restores the image achieving PSNR=313.8596 dB.

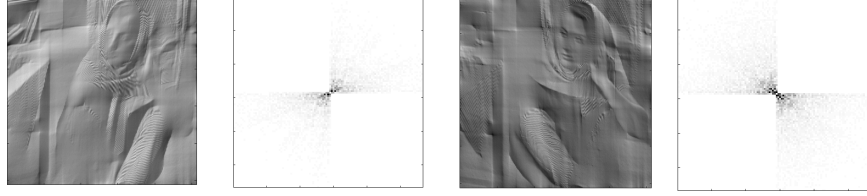


Figure 4.7: Left to right: 1. Partially restored “Barbara” image by $\Re(\mathbf{X}_+)$. 2. Magnitude DFT spectrum of \mathbf{X}_+ . 3. Partially restored image by $\Re(\mathbf{X}_-)$. 4. Magnitude DFT spectrum of \mathbf{X}_- .

4.2.2 Multi-level 2D transforms

It was established in Section 3.4.2 that the 1D qWP transforms of a signal $\mathbf{x} \in \Pi[N]$ to the second and further decomposition levels are implemented by the iterated application of the filter banks that are determined by their analysis modulation matrices $\tilde{\mathbf{M}}[2^m n]$, $m = 1, \dots, M - 1$, to the coefficient arrays $\mathbf{z}_{\pm[m]}^\lambda$. The transforms applied to the arrays $\mathbf{z}_{\pm[m]}^\lambda$ produce the arrays $\mathbf{z}_{\pm[m+1]}^\rho$, respectively. The inverse transform consists of the iterated application of the filter banks that are determined by their synthesis modulation matrices $\mathbf{M}[2^m n]$, $m = 1, \dots, M - 1$, to the coefficient arrays $\mathbf{z}_{\pm[m+1]}^\rho$. In that way, the first-level coefficient arrays $\mathbf{z}_{\pm[1]}^\lambda$, $\lambda = 0, 1$, are restored.

The tensor-product of the 2D transforms of a signal $\mathbf{X} \in \Pi[N, N]$ consists of the subsequent application of the 1D transforms to columns and rows of the signal and coefficient arrays. By application of filter banks, which are determined by the analysis modulation matrix $\tilde{\mathbf{M}}[2n]$ to columns and rows of the coefficient array $\mathbf{Z}_{\pm[1]}^{j,l}$, we derive four second-level arrays $\mathbf{Z}_{\pm[2]}^{\rho,\tau}$, $\rho = 2j, 2j + 1$; $\tau = 2l, 2l + 1$. The arrays $\mathbf{Z}_{\pm[1]}^{j,l}$ are restored by the application of the filter banks that are determined by their synthesis modulation matrices $\mathbf{M}[2n]$ to rows and columns of the coefficient arrays $\mathbf{Z}_{\pm[2]}^{\rho,\tau}$, $\rho = 2j, 2j + 1$; $\tau = 2l, 2l + 1$. The transition from the second to further levels and back are executed similarly using the modulation matrices $\tilde{\mathbf{M}}[2^m n]$ and $\mathbf{M}[2^m n]$, respectively. The inverse transforms produce the coefficient arrays $\mathbf{Z}_{\pm[1]}^{j,l}$, $j, l = 0, 1$, from which the signal $\mathbf{X} \in \Pi[N, N]$ is restored using the synthesis modulation matrices $\mathbf{M}_\pm^q[n]$ as it is explained in Section 4.2.1.

All the computations are implemented in the frequency domain using FFT. For example, the Matlab execution of the 2D qWP transform of a 512×512 image down to the sixth decomposition level takes 0.45 second. The four-level transform takes 0.20 second.

Summary The 2D qWP processing of a signal $\mathbf{X} \in \Pi[N, N]$ is implemented by a dual-tree scheme. The first step produces two sets $\mathbf{Z}_{+[1]}$ and $\mathbf{Z}_{-[1]}$ of the coefficient arrays which are derived

using the analysis modulation matrices $\tilde{\mathbf{M}}_+^q[n]$, and $\tilde{\mathbf{M}}_-^q[n]$, respectively. Further decomposition steps are implemented in parallel on the sets $\mathbf{Z}_{+[1]}$ and $\mathbf{Z}_{-[1]}$ using the same analysis modulation matrix $\tilde{\mathbf{M}}[2^m n]$, thus producing two multi-level sets of the coefficient arrays $\{\mathbf{Z}_{+[m]}^{j,l}\}$ and $\{\mathbf{Z}_{-[m]}^{j,l}\}$, $m = 2, \dots, M$, $j, l = 0, 2^m - 1$.

By parallel implementation of the inverse transforms on the coefficients from the sets $\{\mathbf{Z}_{+[m]}^{j,l}\}$ and $\{\mathbf{Z}_{-[m]}^{j,l}\}$ using the same synthesis modulation matrix $\mathbf{M}[2^m n]$, the sets $\mathbf{Z}_{+[1]}$ and $\mathbf{Z}_{-[1]}$ are restored, which, in turn, provide the signals \mathbf{X}_+ and \mathbf{X}_- , using the synthesis modulation matrices $\mathbf{M}_+^q[n]$ and $\mathbf{M}_-^q[n]$, respectively. Typical signals \mathbf{X}_\pm and their DFT spectra are displayed in Fig. 4.7.

Prior to the reconstruction, some structures, possibly different, are defined in the sets $\{\mathbf{Z}_{+[m]}^{j,l}\}$ and $\{\mathbf{Z}_{-[m]}^{j,l}\}$, $m = 1, \dots, M$, (for example, 2D wavelet, Best Basis or single-level structures) and some manipulations on the coefficients, (for example, thresholding, shrinkage, l_1 minimization) are executed.

5 Image denoising

In this section, we apply the designed directional wavelet packets to the problem of restoring an image \mathbf{X} from the data $\tilde{\mathbf{X}} = \mathbf{X} + \varepsilon_\sigma$, where ε_σ is the Gaussian zero-mean noise whose STD is σ .

5.1 Denoising scheme

The degraded image $\tilde{\mathbf{X}}$ is decomposed into two sets $\{\tilde{\mathbf{Z}}_{+[m]}^{j,l}\}$ and $\{\tilde{\mathbf{Z}}_{-[m]}^{j,l}\}$, $m = 1, \dots, M$, $j, l = 0, 2^m - 1$, of the qWP transform coefficients, then the Bivariate Shrinkage algorithm (BSA)[21, 7] is implemented and the image $\tilde{\mathbf{X}} \approx \mathbf{X}$ is restored from the shrunken coefficients. The experiments demonstrate the ability of the qWPs to restore edges and texture details even from severely degraded images. Certainly, this ability stems from the fact that the designed 2D qWP transforms provide a variety of 2D waveforms oriented in multiple directions, which are spatially localized and have oscillatory structure.

5.1.1 Bivariate Shrinkage

The BSA is applicable to cases when the set of transform coefficients has a tree structure which implies that there is a dependency between the coefficients from different decomposition layers. Such a structure is inherent in the WP transforms with real wavelet packets as well as in the transforms with the complex qWPs $\Psi_{+\pm[m],j,l}^{2r}$. The summary of the BSA is ([21]):

1. Estimation of the noise variance by $\tilde{\sigma}_e^2 = \frac{\text{median}(|c[k,n]|)}{0.6745}$, where $\{c[k,n]\}$ are coefficients in the high-frequency $\{1,1\}$ block from the first decomposition level of the degraded image $\tilde{\mathbf{X}}$.
2. For each transform coefficient $c_m[k,n]$ from the m -th decomposition level:
 - (a) Calculate the averaged variance $\bar{\sigma}_c[k,n]^2 = \frac{1}{O} \sum_{c_m[\kappa,\nu] \in \Omega[k,n]} c_m[\kappa,\nu]^2$, where $\Omega[k,n]$ is a neighborhood of the coefficient $c_m[k,n]$ and O is cardinality of $\Omega[k,n]$.

- (b) The marginal variance for the coefficient $c_m[k, n]$ is estimated: $\tilde{\sigma}[k, n]^2 = (\bar{\sigma}_c[k, n]^2 - \tilde{\sigma}_e^2)_+$. Here $\xi_+ = \begin{cases} \xi & \text{if } \xi > 0; \\ 0, & \text{otherwise.} \end{cases}$
- (c) The transform coefficient $C_m[k, n]$ of the clean image \mathbf{X} is estimated by

$$C_m[k, n] \approx \tilde{C}_m[k, n] = \frac{\left(\sqrt{c_m[k, n]^2 + \check{c}_{m+1}[k, n]^2} - \frac{\sqrt{3}\tilde{\sigma}_e^2}{\tilde{\sigma}[k, n]} \right)_+}{\sqrt{c_m[k, n]^2 + \check{c}_{m+1}[k, n]^2}} c_m[k, n], \quad (5.1)$$

where $\check{c}_{m+1}[k, n]$ is the transform coefficient from the coarser decomposition level which is located at approximately the same spatial position as the coefficient $c_m[k, n]$ and, in our case, is related to the waveform with approximately the same directionality as the waveform related to $c_m[k, n]$.

3. Application of the inverse transform to the coefficients \mathbf{C} .

5.1.2 Implementation of an image denoising with qWP transforms

The proposed denoising algorithm, which we refer to as qWPA, is implemented via the following steps:

1. In order to eliminate boundary effects, the degraded image $\tilde{\mathbf{X}}$ of size $N \times N$ is symmetrically extended to image $\tilde{\mathbf{X}}_T$ of size $N_1 \times N_1$, where $N_1 = N + 2T$. Typically $T = N/8$.
2. The direct 2D transforms of the image $\tilde{\mathbf{X}}_T$ with the complex qWPs $\Psi_{++[m],j,l}^{2r}$ and $\Psi_{+-[m],j,l}^{2r}$, $m = 1, \dots, 5$ are executed down to the fifth decomposition level. As a result, two sets $\{\tilde{\mathbf{Z}}_{+[m]}^{j,l}\}$ and $\{\tilde{\mathbf{Z}}_{-[m]}^{j,l}\}$, $m = 1, \dots, 5$, $j, l = 0, \dots, 2^m - 1$, of the qWP transform coefficients are produced.
3. The noise variance is estimated by $\tilde{\sigma}_e^2 = \frac{\text{median}(|\tilde{Z}_{+[1]}^{1,1}[k, n]|)}{0.6745}$.
4. $\check{c}_4[k, n] \stackrel{\text{def}}{=} \tilde{Z}_{+[4]}^{j,l}[k, n]$ denotes a coefficient from the block $\tilde{\mathbf{Z}}_{+[4]}^{j,l}$ in the fourth decomposition level. The following operations are applied to the coefficient $\check{c}_4[k, n]$:
 - (a) The averaged variance $\bar{\sigma}_c[k, n]^2 = \frac{1}{W_4^2} \sum_{\kappa, \nu=-W_4/2}^{W_4/2-1} \check{c}_4[k + \kappa, n + \nu]^2$ is calculated. The number W_4 determines the neighborhood $\Omega_4[k, n]$ size.
 - (b) The marginal variance for the coefficient $\check{c}_4[k, n]$ is estimated by $\tilde{\sigma}[k, n]^2 = (\bar{\sigma}_c[k, n]^2 - \tilde{\sigma}_e^2)_+$.
 - (c) In order to estimate the clean transform coefficients from the fourth decomposition level, according to Eq. (5.1), it is needed to utilize the coefficients from the fifth level. The size of the block $\tilde{\mathbf{Z}}_{+[4]}^{j,l}$ of transform coefficients is $N_1/16 \times N_1/16$. The coefficients from that block are related to the qWP $\Psi_{++[4],j,l}^{2r}$, whose spectrum occupies, approximately, a square $\mathbf{S}_{+[4]}^{j,l}$ of size $N_1/32 \times N_1/32$ within the quadrant \mathbf{Q}_0 . The spectrum's location determines the directionality of the waveform $\Psi_{++[4],j,l}^{2r}$. On the other hand, four coefficient blocks $\{\tilde{\mathbf{Z}}_{+[5]}^{2j+\iota, 2l+\lambda}\}$, $\iota, \lambda = 0, 1$, of size $N_1/32 \times N_1/32$ are derived by filtering the block $\tilde{\mathbf{Z}}_{+[4]}^{j,l}$ followed by downsampling. The coefficients from those blocks are

related to the qWPs $\Psi_{++[5],2j+\iota,2l+\lambda}^{2r}$, whose spectra occupy, approximately, the squares $\mathbf{S}_{+[5]}^{2j+\iota,2l+\lambda}$ of size $N_1/64 \times N_1/64$, which fill the square $\mathbf{S}_{+[4]}^{j,l}$. Therefore, the orientations of the waveforms $\Psi_{++[5],2j+\iota,2l+\lambda}^{2r}$ are close to the orientation of $\Psi_{++[4],j,l}^{2r}$. Keeping this in mind, we form the joint fifth-level array $\mathbf{c}_5^{j,l}$ of size $N_1/32 \times N_1/32$ by interleaving the coefficients from the arrays $\{\check{\mathbf{Z}}_{+[5]}^{2j+\iota,2l+\lambda}\}$. To be specific, the joint array $\mathbf{c}_5^{j,l}$ consists of the quadruples:

$$\mathbf{c}_5^{j,l} = \left\{ \begin{bmatrix} \check{Z}_{+[5]}^{2j,2l}[2k, 2n] & \check{Z}_{+[5]}^{2j,2l+1}[2k, 2n] \\ \check{Z}_{+[5]}^{2j+1,2l}[2k, 2n] & \check{Z}_{+[5]}^{2j+1,2l+1}[2k, 2n] \end{bmatrix} \right\}, \quad k, n = 0, \dots, N_1/32 - 1. \quad (5.2)$$

- (d) Let $\check{c}_5[k, n]$ denote a coefficient from the joint array $\mathbf{c}_5^{j,l}$. Then, the clean transform coefficients $C_{+[4]}^{j,l}[k, n]$ from the fourth decomposition level are estimated by

$$C_{+[4]}^{j,l}[k, n] \approx \tilde{C}_{+[4]}^{j,l}[k, n] = \frac{\left(\sqrt{\check{c}_4[k, n]^2 + \check{c}_5[k, n]^2} - \frac{\sqrt{3}\check{\sigma}_e^2}{\check{\sigma}[k, n]} \right)_+}{\sqrt{\check{c}_4[k, n]^2 + \check{c}_5[k, n]^2}} \check{c}_4[k, n]. \quad (5.3)$$

- (e) As a result of the above operations, the estimated fourth-level coefficients of the clean image $\tilde{\mathbf{Z}}_{+[4]} = \{\tilde{\mathbf{Z}}_{+[4],j,l}\}$, $j, l = 0, \dots, 15$, are derived where the coefficient block $\tilde{\mathbf{Z}}_{+[4],j,l} = \{\tilde{C}_{+[4]}^{j,l}[k, n]\}$, $k, n = 0, \dots, N_1/16 - 1$.

- (f) The inverse qWP transform is applied to the coefficient array $\tilde{\mathbf{Z}}_{+[4]}$ and the result shrinks to the original image size $N \times N$. Thus, the sub-image $\tilde{\mathbf{X}}_+^4$ is obtained.

5. Let $\check{c}_3[k, n] \stackrel{\text{def}}{=} \check{Z}_{+[3]}^{j,l}[k, n]$ denotes a coefficient from the block $\check{\mathbf{Z}}_{+[4]}^{j,l}$ in the third decomposition level. The operations, which are similar to those in Item 4, are applied to on the coefficient $\check{c}_3[k, n]$.

- (a) The averaged variance $\bar{\sigma}_c[k, n]^2 = \frac{1}{W_3^2} \sum_{\kappa, \nu=-W_3/2}^{W_3/2-1} \check{c}_3^+[k + \kappa, n + \nu]^2$ is calculated. Typically, the number $W_3 \neq W_4$.
- (b) The clean transform coefficients $C_{+[3]}^{j,l}[k, n]$ from the third decomposition level are estimated by

$$C_{+[3]}^{j,l}[k, n] \approx \tilde{C}_{+[3]}^{j,l}[k, n] = \frac{\left(\sqrt{\check{c}_3[k, n]^2 + \check{c}_4[k, n]^2} - \frac{\sqrt{3}\check{\sigma}_e^2}{\check{\sigma}[k, n]} \right)_+}{\sqrt{\check{c}_3[k, n]^2 + \check{c}_4[k, n]^2}} \check{c}_3[k, n]. \quad (5.4)$$

- (c) The difference with the previous case is that the joint fourth-level array $\mathbf{c}_4^{j,l}$ of size $N_1/16 \times N_1/16$ is formed from already “cleaned” coefficients from the fourth level:

$$\mathbf{c}_4^{j,l} = \left\{ \begin{bmatrix} \tilde{C}_{+[4]}^{2j,2l}[2k, 2n] & \tilde{C}_{+[4]}^{2j,2l+1}[2k, 2n] \\ \tilde{C}_{+[4]}^{2j+1,2l}[2k, 2n] & \tilde{C}_{+[4]}^{2j+1,2l+1}[2k, 2n] \end{bmatrix} \right\}, \quad k, n = 0, \dots, N_1/16 - 1. \quad (5.5)$$

- (d) As a result of the above operations, the estimated third-level coefficients of the clean image: $\tilde{\mathbf{Z}}_{+[3]} = \{\tilde{\mathbf{Z}}_{+[3],j,l}\}$, $j, l = 0, \dots, 7$ are derived, where the coefficient block is $\tilde{\mathbf{Z}}_{+[3],j,l} = \{\tilde{C}_{+[3]}^{j,l}[k, n]\}$, $k, n = 0, \dots, N_1/8 - 1$.

- (e) The inverse qWP transform is applied to the coefficient array $\tilde{\mathbf{Z}}_{+[3]}$ and the result shrinks to the original image size $N \times N$. Thus the sub-image $\tilde{\mathbf{X}}_+^3$ is obtained.
6. The same operations as in Items 4 and 5 are applied to the coefficient array $\{\tilde{\mathbf{Z}}_{-[m]}^{j,l}\}$, $m = 1, \dots, 5$, $j, l = 0, \dots, 2^m - 1$. After the application of the inverse transforms the sub-images $\tilde{\mathbf{X}}_-^4$ and $\tilde{\mathbf{X}}_-^3$ are derived.
7. The images that approximate the clean image are derived by combining the sub-images:

$$\tilde{\mathbf{X}}^4 = \frac{\tilde{\mathbf{X}}_+^4 + \tilde{\mathbf{X}}_-^4}{8}, \quad \tilde{\mathbf{X}}^3 = \frac{\tilde{\mathbf{X}}_+^3 + \tilde{\mathbf{X}}_-^3}{8}.$$

8. The final operation is formed by the weighted average

$$\tilde{\mathbf{X}} = \frac{a \tilde{\mathbf{X}}^3 + b \tilde{\mathbf{X}}^4}{a + b}. \quad (5.6)$$

Remark 5.1 *Matlab implementation of all the operations listed in Items 1–8 on an image of size 512×512 pixels takes 0.8 seconds. Note that the noise STD is not a part of the input. It is evaluated as indicated in Item 3.*

Remark 5.2 *In some cases, especially when images are severely damaged by the presence of a strong noise, it has been demonstrated that using the second-level WPs is useful. In these cases, the image $\tilde{\mathbf{X}}^2$ is produced in addition to images $\tilde{\mathbf{X}}^3$ and $\tilde{\mathbf{X}}^4$. Then, the approximated image is formed by*

$$\tilde{\mathbf{X}} = \frac{a \tilde{\mathbf{X}}^3 + b \tilde{\mathbf{X}}^4 + c \tilde{\mathbf{X}}^2}{a + b + c}. \quad (5.7)$$

Matlab implementation takes 1.2 seconds.

Remark 5.3 *The algorithm comprises a number of free parameters which enable a flexible adaptation to the processed object. Such parameters are the order $2r$ of the generating discrete spline, numbers W_4 and W_3 (and W_2 when the second-level WPs are involved), which determine the sizes of neighborhoods for the averaged variances calculation, and the weights a and b in Eq. (5.6) (a, b, c in Eq. (5.7)).*

Remark 5.4 *The Matlab functions `denoising_dwt.m` and `bishrink.m` from the websites http://eeweb.poly.edu/iselesni/WaveletSoftware/denoising_dwt.html and <http://eeweb.poly.edu/iselesni/WaveletSoftware/denoise2.html>, respectively, were used.*

5.2 Experimental results

In this section, we compare the performance of our denoising algorithm designated as qWPA on restoration of degraded benchmark images with the performances of state-of-the-art algorithms such as *Block-matching and 3D filtering (BM3D)* ([8], *Directional Compactly Supported Tensor Product Complex Tight Framelets (cptTP-CTF₆)* ([26]) and *Digital Affine Shear Filter Transform with 2-Layer Structure (DAS-2)* ([6]). To produce results for the comparison, we used the software available at the websites http://www.cs.tut.fi/~foi/GCF-BM3D/index.html#ref_software (BM3D)

and

<http://staffweb1.cityu.edu.hk/xzhuang7/softs/index.html#bdTPCTF> (cptTP- CTF_6 and DAS-2).

The restored images were evaluated by visual perception, by Peak Signal-to-Noise ratio (PSNR) (see Eq. (1.4)) and by the Structural Similarity Index (SSIM) ([24], `ssim.m` Matlab function). The SSIM measures the structural similarity of small moving windows in two images. It varies from 1 for fully identical windows to -1 for completely dissimilar ones. The SSIM map visualizes the local index values for all the images' pixels while the global index is the average of the local indices. Currently, the SSIM is regarded as more informative characteristics of the image quality compared to PSNR and Mean Square Error (MSE).

For the experiments, we used a standard set of benchmark images: "Lena", "Boat", "Barbara", and "Fingerprint". The "clean" images are displayed in Fig. 5.1.



Figure 5.1: Clean images: "Lena", "Boat", "Barbara" and "Fingerprint"

The images were corrupted by a Gaussian zero-mean noise whose STD was σ . Then, the qWPA, BM3D, cptTP- CTF_6 and DAS-2 denoising algorithms were applied to restore the images. The restoration results were evaluated by the PSNR and SSIM values. Table 5.1 presents the results of "Lena" image restoration and Fig. 5.2 illustrates the SSIM results.

1	2	3	4	5	6
σ	noised	qWPA	cptTP-CTF ₆	DAS-2	BM3D
5	34.19/0.65	38.27/ 0.7298	38.4/0.7050	38.31/0.7272	38.75 /0.7078
10	28.17/0.43	35.33/ 0.6335	35.49/0.6160	35.24/0.6250	35.96 /0.6233
25	20.21/0.2	31.19/ 0.5034	31.56/0.4992	31.12/0.4920	32.11 /0.5026
40	16.13/0.12	29.03/ 0.4332	29.45/0.4313	28.94/0.4148	29.9 /0.4265
50	14.19/0.09	27.99/ 0.3967	28.45/0.3965	27.87/0.3757	29.08 /0.3957
80	10.11/0.04	25.92/0.3187	26.39/0.3199	25.56/0.290	27.0/0.3214
100	8.17/0.03	24.87/0.2812	25.45/0.2833	24.43/0.2285	25.99/0.2851

Table 5.1: PSNR/SSIM values for restoration of “Lena” image. Boldface highlights the best results

Table 5.1 and Fig. 5.2 demonstrate that although the BM3D and cptTP-CTF₆-restored images achieve the higher PSNR compared to the qWPA, this is not the case for the SSIM values. In particular, the best SSIM is achieved by the qWPA when noise STD is $\sigma = 5, 10, 25, 40$ and 50 dB.

Table 5.2 presents the results for the “Boat” image restoration and Fig. 5.2 illustrates the SSIM results.

1	2	3	4	5	6
σ	noised	qWPA	cptTP-CTF ₆	DAS-2	BM3D
5	34.19/0.7855	36.29/0.7919	36.89/0.8044	36.89/ 0.8294	37.2 /0.8065
10	28.17/0.58	33.21/ 0.7001	33.38/0.6713	33.18/0.6880	33.95 /0.6805
25	20.21/0.29	28.94/ 0.53	29.16/0.5040	28.92/0.5182	29.94 /0.5296
40	16.13/0.18	26.83/0.435	27.05/0.4044	26.81/0.4228	27.77/0.4395
50	14.19/0.13	25.87/0.3889	26.12/0.3567	25.85/0.3763	26.81/0.3899
80	10.11/0.07	23.96/ 0.2953	24.31/0.2626	23.87/0.2792	24.9 /0.2952
100	8.17/0.05	23.05/ 0.2543	23.52/0.2232	22.93/0.2361	24.0 /0.2533

Table 5.2: PSNR/SSIM values for restoration of “Boat” image. Boldface highlights the best results

Table 5.2 and Fig. 5.2 show that, again, BM3D-restored images achieved the best PSNR results in almost all cases. As for the qWPA, the SSIM values are the best when the STDs are $\sigma = 10, 25, 80$ and 100 dB.

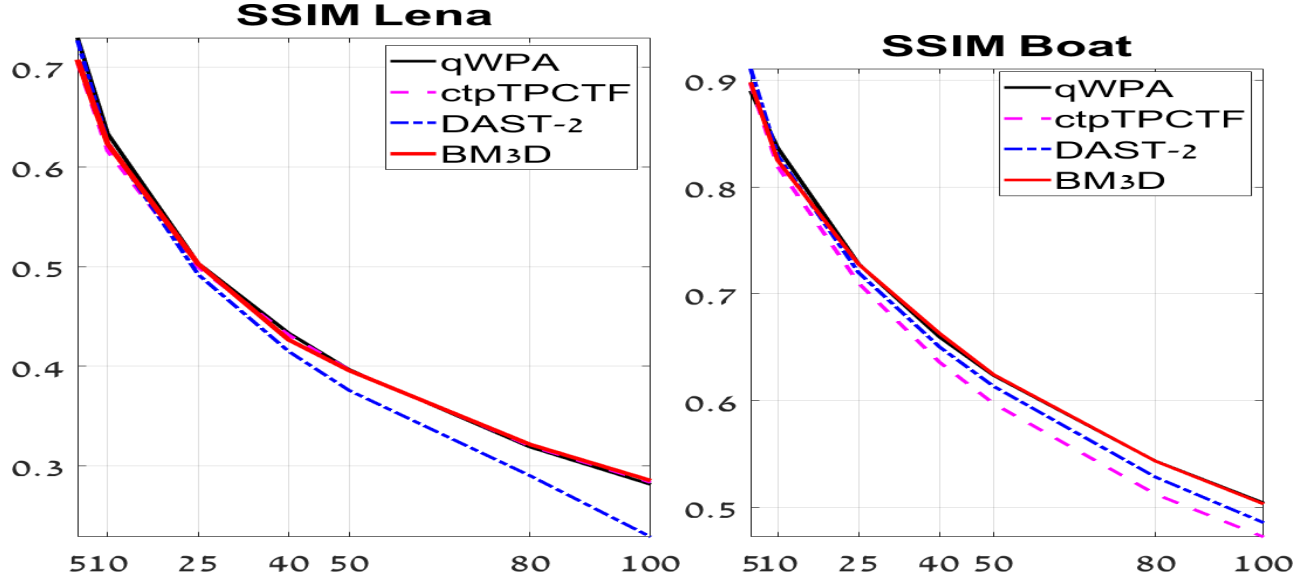


Figure 5.2: Restoration of “Lena” (left) and “Boat” (right) images: comparison of four denoising methods – SSIM values

Table 5.3 presents the results for the “Barbara” image restoration and Fig. 5.5 shows the SSIM results.

1	2	3	4	5	6
σ	noised	qWPA	cptTP-CTF ₆	DAS-2	BM3D
5	34.19/0.77	37.96/ 0.8441	37.75/0.8382	37.71/0.8438	38.34 /0.8387
10	28.17/0.6	34.54/ 0.7761	34.07/0.763	34.01/0.764	35.01 /0.7738
25	20.21/0.35	29.85/0.6566	29.28/0.6358	29.43/0.6422	30.75 / 0.6707
40	16.13/0.23	27.57/ 0.5789	26.78/0.5375	27.13/0.5595	28.02 /0.5788
50	14.19/0.18	26.50/0.5340	25.64/0.4833	26.04/0.5121	27.26 / 0.5389
80	10.11/0.09	24.29/ 0.4268	23.47/0.3633	23.76/0.3987	24.82 /0.4192
100	8.17/0.06	23.26/ 0.3723	22.59/0.3092	22.67/0.3398	23.66 /0.3608

Table 5.3: PSNR/SSIM values for restoration of “Barbara” image. Boldface highlights the best results

Table 5.3 and Fig. 5.5 show that, although BM3D achieves the highest PSNR for the restored images, in almost all the cases the best SSIM is achieved by qWPA. Note that in all the cases, the qWPA achieved higher PSNR compared to cptTP-CTF₆ and DAS-2.

Figure 5.3 illustrates the restoration results for “Barbara” image corrupted by Gaussian noise with $\sigma = 40$ dB. Restoration by qWPA is compared with the output from BM3D. For reference, the clean and corrupted images are displayed in the figure. Major part of the fine texture is completely destroyed in the noised image. Table 5.3 shows that the SSIM values for generated by qWPA and BM3D methods are almost the same but BM3D achieves higher PSNR. Both methods succeeded in eliminating noise and restore a significant part of the texture. However, the image that was restored by BM3D looks over-smoothed. This observation is confirmed by images displayed in Fig.

5.4.

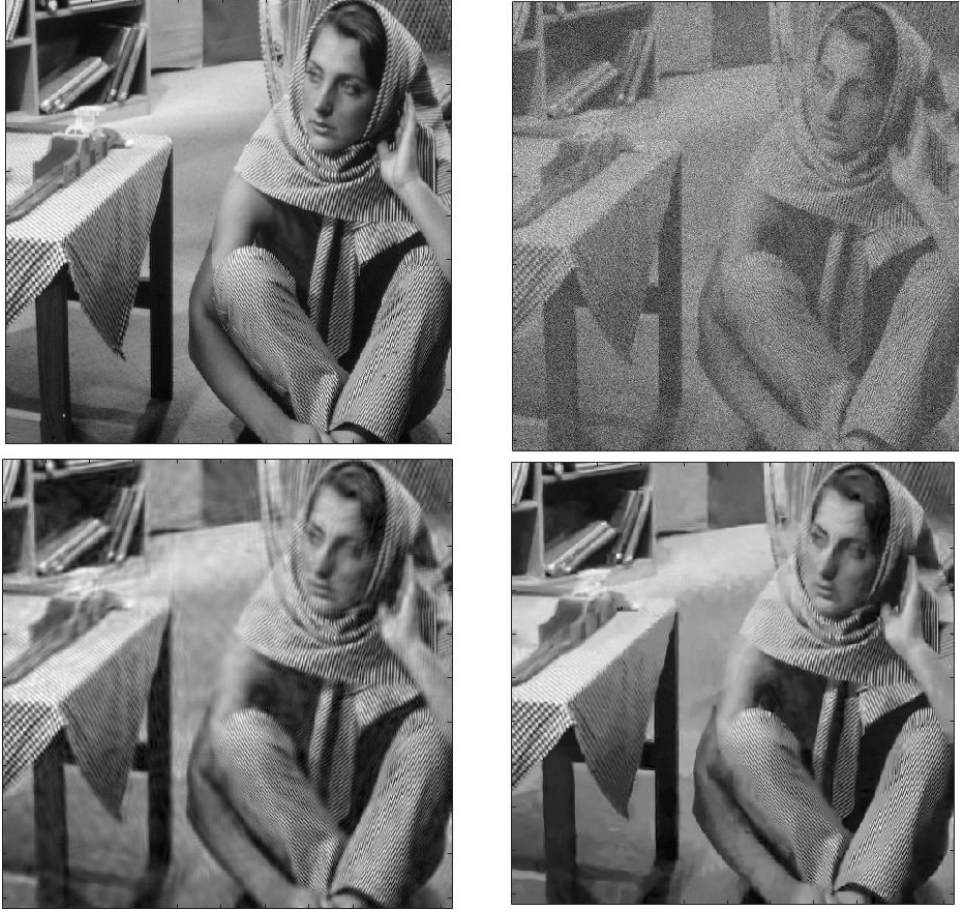


Figure 5.3: Restoration of “Barbara” image. Top left: clean image. Top right: image corrupted by Gaussian noise with $\sigma = 40$ dB, PSNR=16.3 dB, SSIM=0.23. Bottom left: Restoration by qWPA, PSNR=27.56 dB, SSIM=0.5789. Bottom right: Restoration by BM3D, PSNR=28.02 dB, SSIM=0.5788

The two top pictures in Fig. 5.4 display colored SSIM maps for the images restored by qWPA and BM3D methods, respectively. The pictures show that, within the selected squares, the structure similarity index in the image restored by qWPA is higher than what was restored by BM3D (tablecloth and part of the leg). The two bottom pictures display fragments of the restored images related to the selected squares. In the patches marked by ellipses, the qWPA succeeded in restoring at least traces of the fine texture, while the BM3D fails.

Table 5.4 presents the results of the “Fingerprint” image restoration and Fig. 5.5 illustrates the SSIM results.

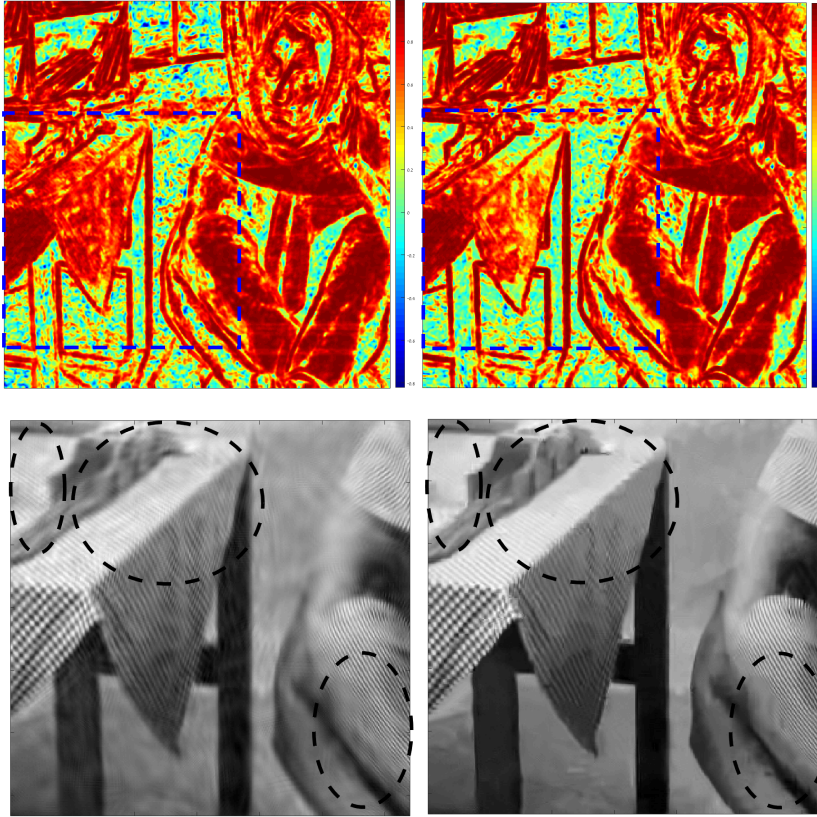


Figure 5.4: Restoration of “Barbara” image. Top left: SSIM map for image restored by qWPA. Top right: SSIM map for image restored by BM3D. The blue square indicates the area where the performance of qWPA is better than BM3D. Bottom left: fragment of the image restored by qWPA. Bottom right: fragment of the image restored by BM3D.

1	2	3	4	5	6
σ	noised	qWPA	cptTP-CTF ₆	DAS-2	BM3D
5	34.19/0.97	36.58 /0.9852	36.30/0.9845	36.29/0.9843	36.54/ 0.9854
10	28.17/0.91	32.46/ 0.96343	32.40/0.9625	32.06/0.9601	32.49 /0.96338
25	20.21/0.67	27.48/ 0.8984	27.37/0.889	27.11/0.886	27.74 /0.8955
40	16.13/0.48	25.19/ 0.8340	25.10/0.8219	24.9/0.8246	25.34 /0.8334
50	14.19/0.38	24.25/ 0.8024	24.08/0.7815	23.91/0.7895	24.56 /0.8019
80	10.11/0.21	22.16/ 0.7236	22.02/0.6746	21.91/0.7013	22.59 /0.7165
100	8.17/0.15	21.33/ 0.6848	21.06/0.6129	20.99/0.6520	21.65 /0.6643

Table 5.4: PSNR/SSIM values for restoration of “Fingerprint” image. Boldface indicate the best results

Table 5.4 and Fig. 5.5 show that, although BM3D achieves the highest PSNR for all the restored images, except for $\sigma = 5$, in all the cases, except for $\sigma = 5$, the best SSIM is achieved by qWPA. As in the previous example, in all the cases, the qWPA achieved higher PSNR compared to cptTP-CTF₆ and DAS-2.

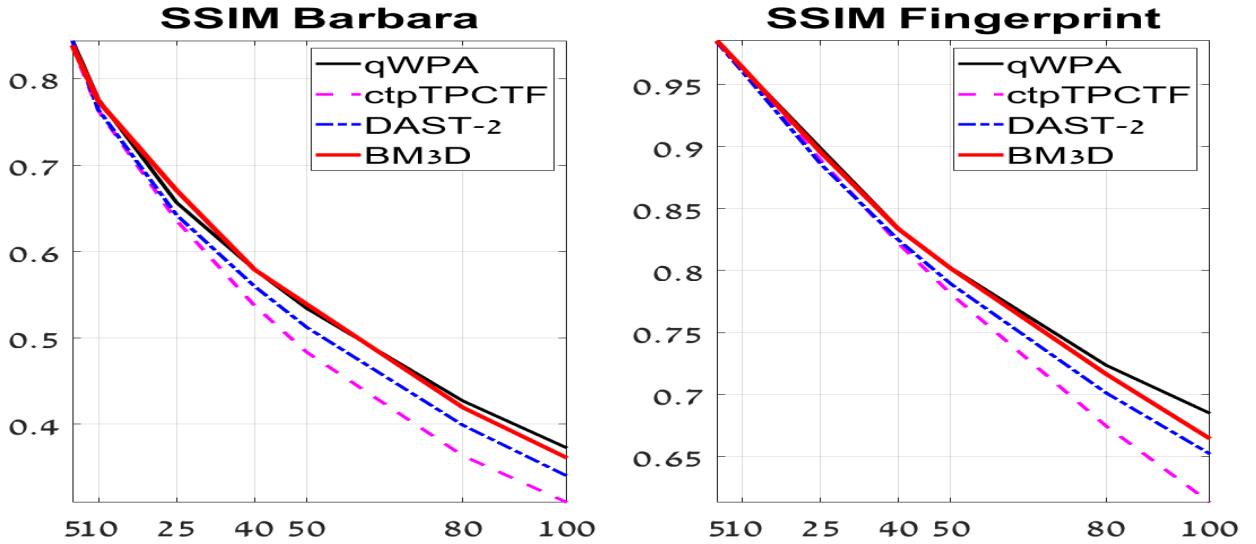


Figure 5.5: Restoration of “Barbara” (left) and “Fingerprint” (right) images: comparison of four denoising methods – SSIM values

Figure 5.6 illustrates the results of the restoration of “Fingerprint” corrupted by a strong Gaussian noise with $\sigma = 100$ dB. The restoration by qWPA is compared with the restoration by BM3D. For reference, the clean and the corrupted images are displayed in the figure. Characteristic features of fingerprint image are almost completely buried in the noise. Table 5.3 shows that the SSIM value that qWPA generates is higher than what BM3D generates but BM3D generates higher PSNR. Both methods succeeded to eliminate noise and restore a significant part of the image. However, the BM3D fails to restore some patches in the image. This observation is illustrated by the images

in Fig. 5.7.

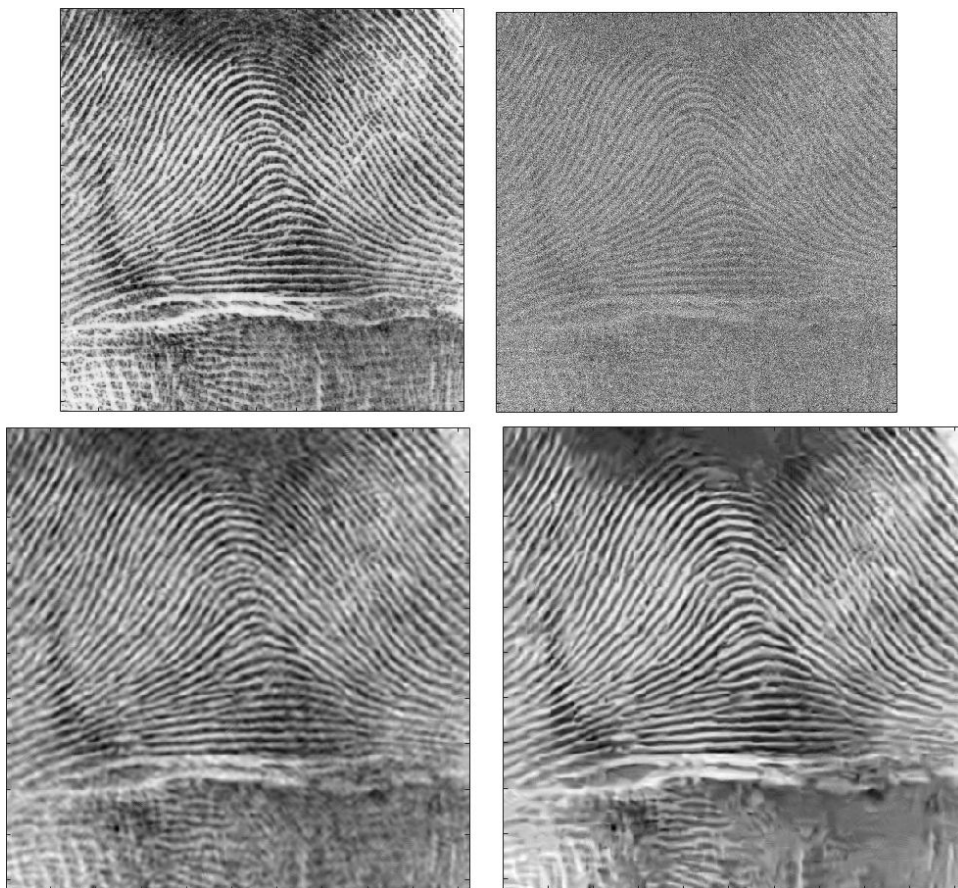


Figure 5.6: Restoration of “Fingerprint” image. Top left: clean image. Top right: image corrupted by Gaussian noise with $\sigma = 100$ dB, PSNR=8.17 dB, SSIM=0.15. Bottom left: Restoration by qWPA, PSNR=21.52 dB, SSIM=0.6685. Bottom right: Restoration by BM3D, PSNR=21.65 dB, SSIM=0.6643

The two top pictures in Fig. 5.7 display colored SSIM maps for images restored by qWPA and BM3D methods, respectively. Within the selected squares, the structure similarity index in the image restored by qWPA is higher than what BM3D restores (top and bottom-right parts of the images). The four bottom pictures display fragments of the restored images related to the selected squares. In these fragments, the qWPA succeeded in restoring at least traces of the structure, while the BM3D completely failed to restore significant patches.

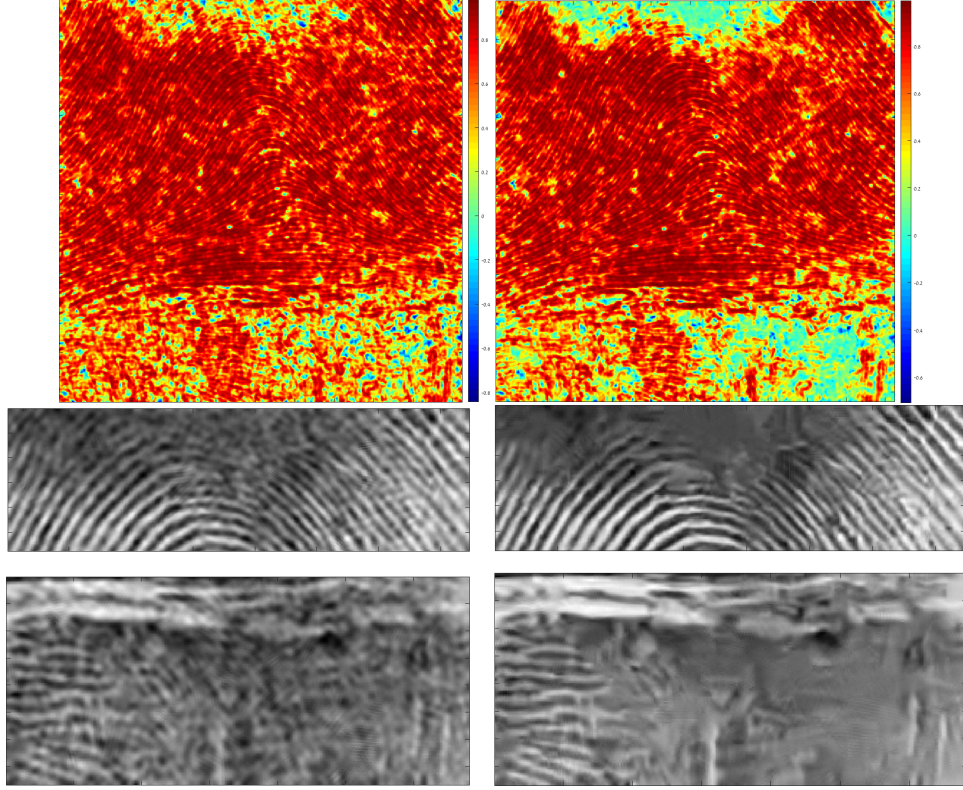


Figure 5.7: Restoration of “Fingerprint” image. Top left: SSIM map for restoration by qWPA. Top right: SSIM map for restoration by BM3D. The blue square indicates the area where qWPA has better performance over BM3D. Bottom left: fragments from restoration by qWPA. Bottom right: fragments from restoration by BM3D.

6 Inpainting

6.1 Methodology

Method1 and Method2 are two qWP-based methods that are applied to image inpainting. Image inpainting means restoration of an image that was degraded by having many missing pixels and corrupted by Gaussian noise. Both methods rely on the redundancy of the qWP transforms and on the interdependency of the transform coefficients in the horizontal (between neighboring coefficients) and vertical (parent-child) directions. As in the denoising section 5, this interdependency is utilized via the Bivariate Shrinkage algorithm (BSA) ([21, 7]), which is outlined in Section 5.1.1.

Further on, we refer to the set of the filter banks DAS-2, DAS-1, TP-CTF₆ and TP-CTF₆[↓] as SET-4.

6.1.1 Method1

This method is a slight modification of the inpainting **Algorithm I** introduced in [22, 23]. **Algorithm I** that uses TP-CTF₆ produces excellent image inpainting results that outperform (in a PSNR sense) most state-of-the-art methods (see [22] for methods comparison). **Algorithm I**

in [6] is implemented using the SET-4 filter banks. On the cartoon images such as “Lena” and “Boat”, TP-CTF₆ achieves better performance than the rest of the members in SET-4. However, the images with texture such as “Fingerprint” and, especially, “Barbara” are inpainted better by the filter bank DAS-2 with increased directionality compared to TP-CTF₆. **Algorithm I**, which is described in detail in [22, 23], consists of iterative thresholding of the transform coefficients with decreasing localized thresholds. After setting a few parameters, the threshold levels are determined automatically using BSA. In Method1, qWP transforms are used instead of applying SET-4 filter banks. As in the denoising scheme in Section 5.1.2, the results from the third and fourth decomposition levels are combined. Due to multiple orientations (30 at the third level and 62 at the fourth level) and due to the oscillatory structure of testing waveforms, Method1 outperforms in both PSNR and SSIM all the SET-4 algorithms when applied to “Barbara” and “Fingerprint” images. Although for “Lena” and “Boat” images, the SET-4 algorithms produce the highest PSNR values, in many experiments with “Lena” and almost all the experiments with “Boat”, the SSIM outputs from Method1 exceed those from SET-4.

6.1.2 Method2

In [2] and Chapter 18 in [4], image restoration scheme is developed utilizing the 2D wavelet frames designed in Chapter 17 of [4]. A few restoration examples are presented in [1], where the same scheme as in [4] is used with replacement of wavelet frames by the directional qWPs. This replacement improves the restoration results. Images are restored in [4, 1] by the application of the *split Bregman iteration* (SBI) scheme [9] that uses the so-called *analysis-based* approach (see for example [16]).

Method2 to be described couples Method1 with the SBI scheme. In essence, it is the SBI algorithm supplied with decreasing localized thresholds determined by BSA.

Standard SBI scheme: $\mathbf{u} = \{u[\kappa, \nu]\}$ denotes the original image array to be restored from the degraded array

$$\mathbf{P}_\Theta \mathbf{f} = \mathbf{P}_\Theta (\mathbf{K} \mathbf{u} + \varepsilon), \quad (6.1)$$

where $\varepsilon = \{e_{k,n}\}$ is the i.i.d. Gaussian error array, \mathbf{K} denotes the operator of 2D discrete convolution of the array \mathbf{u} with a kernel $\mathbf{k} = \{k[\kappa, \nu]\}$ and \mathbf{P}_Θ denotes the projection operator on the available set of pixels. This operator can be expressed via the application of a mask Θ to an image \mathbf{x} . The mask Θ is a matrix of the same size as \mathbf{x} , which consists of ones and zeros. Ones indicate the places of available pixels.

The solution scheme is based on the assumption that the original image \mathbf{u} can be sparsely represented in the transform (for example, frame or qWP) domain.

Denote by $\tilde{\mathbf{F}}$ the transform operator of the image \mathbf{u} and $\mathbf{C} \stackrel{\text{def}}{=} \tilde{\mathbf{F}} \mathbf{u}$ is the set of the transform coefficients. Denote by \mathbf{F} the reconstruction operator of the image \mathbf{u} from the set of the transform coefficients, that is $\mathbf{F} \mathbf{C} = \mathbf{u} \iff \mathbf{F} \tilde{\mathbf{F}} = \mathbf{I}$, where \mathbf{I} is the identity operator.

An approximate solution to Eq. (6.1) is derived via minimization of the functional

$$\min_u \frac{1}{2} \|\mathbf{P}_\Theta (\mathbf{K} \mathbf{u} - \mathbf{f})\|_2^2 + \lambda \|\tilde{\mathbf{F}} \mathbf{u}\|_1, \quad (6.2)$$

where $\|\cdot\|_1$ and $\|\cdot\|_2$ are the l_1 and the l_2 norms of the sequences, respectively. Denote by \mathbf{T}_ϑ the

operator of the soft thresholding]

$$\mathbf{T}_\vartheta \mathbf{x} = \{x_\vartheta[\kappa, \nu]\}, \quad x_\vartheta[\kappa, \nu] \stackrel{\text{def}}{=} \text{sgn}(x[\kappa, \nu]) \max\{0, |x[\kappa, \nu]| - \vartheta\}.$$

The minimization problem in Eq. (6.2) is solved by the application of the SBI algorithm (see [16]) in the following way:

Initialization: $\mathbf{u}^0 = 0$, $\mathbf{d}^0 = \mathbf{b}^0 = 0$. Then,

$$\begin{aligned} \mathbf{u}^{k+1} &:= (\mathbf{K}^* \mathbf{P}_\Theta \mathbf{K} + \mu \mathbf{I}) \mathbf{u} = \mathbf{K}^* \mathbf{P}_\Theta \mathbf{f} + \mu \mathbf{F} (\mathbf{d}^k - \mathbf{b}^k), \\ \mathbf{d}^{k+1} &= \mathbf{T}_{\lambda/\mu}(\tilde{\mathbf{F}} \mathbf{u}^{k+1} + \mathbf{b}^k), \\ \mathbf{b}^{k+1} &= \mathbf{b}^k + (\tilde{\mathbf{F}} \mathbf{u}^{k+1} - \mathbf{d}^{k+1}). \end{aligned} \quad (6.3)$$

The linear system in the first line of Eq. (6.3) is solved by the application of the *conjugate gradient* algorithm. The operations in the second and third lines are straightforward. The choice of the parameters λ and μ depend on the experimental conditions.

Description of Method2: In the paper, we do not use the convolution operator in the restoration scheme, thus, $\mathbf{K} = \mathbf{I}$.

Thresholding parameters λ : Assume that the image to be restored comprises M pixels while L pixels are missing. Denote by $\rho = L/M$ the percentage of missing pixels. Similarly to **Algorithm I** in [22], Method2 uses decreasing thresholding values that are determined by the sequences $\Lambda_1[i]$ and $\Lambda_2[i]$ described in Eq. (6.5). Assume that the noise STD= σ is known. Let $\lambda_{\max} \stackrel{\text{def}}{=} 512$,

$$\lambda_{\min} \stackrel{\text{def}}{=} \max \left\{ 1, \sigma \left(1 - \frac{\rho^2}{2} \right) \right\}, \quad \lambda_{\text{mid}} \stackrel{\text{def}}{=} \min \{ \max \{ 2 \lambda_{\min} + 10 \}, 20 \}. \quad (6.4)$$

Let $r_1 \stackrel{\text{def}}{=} \lambda_{\text{mid}}/\lambda_{\max} < 1$, $r_2 \stackrel{\text{def}}{=} \lambda_{\min}/\lambda_{\text{mid}} < 1$. The sequences $\Lambda_1[i]$ and $\Lambda_2[i]$ are defined by

$$\Lambda_1[i] = \sqrt{2} r_1^{\frac{i-R_1}{R_1-1}} \lambda_{\text{mid}}, \quad i = 1, \dots, R_1, \quad \Lambda_2[i] = \sqrt{2} r_2^{\frac{i-R_2}{R_2}} \lambda_{\min}, \quad i = 1, \dots, R_2 \quad (6.5)$$

where R_1 and R_2 are free parameters. In our experiments, we use $R_1 = 5$, $R_2 = 8$.

Bivariate shrinkage operator: Assume that $c_m[k, n]$ is a transform coefficient from a decomposition level m . As in Section 5.1.2, the averaged variance

$$\bar{\sigma}_W[k, n]^2 = \frac{1}{W^2} \sum_{\kappa, \nu=-W/2}^{W/2-1} c_m[k + \kappa, n + \nu]^2 \text{ is calculated.}$$

The marginal variance for the coefficient $c[k, n]$ is estimated: $\tilde{\sigma}_W[k, n]^2 = (\bar{\sigma}_W[k, n]^2 - \lambda^2)_+$, where λ is a parameter taken from either the sequence Λ_1 or Λ_2 by the rule explained below.

Then, the BSA operator \mathbf{B}_λ is defined by

$$\begin{aligned} \mathbf{B}_W^\lambda c_m[k, n] &\stackrel{\text{def}}{=} \begin{cases} c_m[k, n] - \lambda_W(c) \frac{c_m[k, n]}{|c_m[k, n]|}, & \text{if } |c_m[k, n]| > \lambda_W(c); \\ 0, & \text{otherwise,} \end{cases} \\ \lambda_W(c) &= \frac{\sqrt{3} \lambda^2}{\tilde{\sigma}_W[k, n] \sqrt{1 + |c_{m+1}[k, n]/c_m[k, n]|^2}}, \end{aligned} \quad (6.6)$$

where $c_{m+1}[k, n]$ is the transform coefficient from the coarser decomposition level $m + 1$ which is located at approximately the same spatial position as the coefficient $c_m[k, n]$ and, in our case, it is related to the waveform with approximately the same directionality as the waveform related to $c_m[k, n]$. If $\mathbf{C}_m = \{c_m[k, n]\}$ is the set of all transform coefficients from the decomposition level m , then $\mathbf{B}_\lambda \mathbf{C}_m$ is the application of the operator \mathbf{B}_W^λ to each coefficient $c_m[k, n] \in \mathbf{C}_m$.

Implementation of image inpainting by Method2: Denote by $\tilde{\mathbf{F}}_m^+$ and $\tilde{\mathbf{F}}_m^-$ the operators of the transform of an image \mathbf{X} with the complex qWPs $\Psi_{++[m],j,l}^{2r}$ and $\Psi_{+-[m],j,l}^{2r}$, respectively, to the coefficients of decomposition level m such that $\tilde{\mathbf{F}}_m^\pm \mathbf{X} = \mathbf{C}_m^\pm$. Denote by \mathbf{F}_m^+ and \mathbf{F}_m^- the reconstruction operators of the images \mathbf{X}_m^\pm from the sets of the transform coefficients \mathbf{C}_m^+ and \mathbf{C}_m^- , respectively: $\mathbf{X}_m^\pm = \mathbf{F}_m^\pm \mathbf{C}_m^\pm$. Denote by \mathbf{F}_m the operator of the full reconstruction of the image from the coefficient array $\mathbf{C}_m = \mathbf{C}_m^+ \cup \mathbf{C}_m^-$:

$$\mathbf{F}_m \mathbf{C}_m = \mathbf{X}_m = \Re(\mathbf{X}_m^+ + \mathbf{X}_m^-)/8. \quad (6.7)$$

- In order to eliminate boundary effects, the degraded image $\tilde{\mathbf{u}}$ of size $N \times N$ is symmetrically extended to the image \mathbf{f} of size $N_1 \times N_1$, where $N_1 = N + 2T$. Typically, $T = N/8$. Similarly, the mask Θ is extended.
- The free parameters values are set in the following way: 1. Order $2r$ of the discrete spline that generates qWPs (typically $2r = 4$ or $2r = 6$); 2. Integers R_1 and R_2 and tolerance parameters tol_1 and tol_2 (typically, $tol_1 = 0.05$ and $tol_2 = 0.01$); 3. Iterations limits L_1 , L_2 and L_3 ; 4. Windows spans W_3 and W_4 for the averaged variance $\bar{\sigma}_W[k, n]$ calculation at the third and fourth decomposition levels, respectively; 5. Balance factors β_3 and $\beta_4 = 1 - \beta_3$; 6. Regularization parameter μ .
- Initialization: Let $\mathbf{v}^0 = 0$, $\mathbf{b}_{+j}^0 = 0$, $\mathbf{b}_{-j}^0 = 0$, $\mathbf{b}_j^0 = \mathbf{b}_{+j}^0 \cup \mathbf{b}_{-j}^0$, $\mathbf{d}_{+j}^0 = 0$, $\mathbf{d}_{-j}^0 = 0$, $\mathbf{d}_j^0 = \mathbf{d}_{+j}^0 \cup \mathbf{d}_{-j}^0$, where $j = 3, 4$. The thresholding parameter is $\lambda = \Lambda_1[1]$. Then, the iterations start

1. Apply the inverse qWP transforms to the arrays $\mathbf{D}_j^k = \mathbf{d}_j^k - \mathbf{b}_j^k$, where $j = 3, 4$

$$\mathbf{V}_3^k \stackrel{\text{def}}{=} \mathbf{F}_3 \mathbf{D}_3^k, \quad \mathbf{V}_4^k \stackrel{\text{def}}{=} \mathbf{F}_4 \mathbf{D}_4^k, \quad \mathbf{V}^k \stackrel{\text{def}}{=} \beta_3 \mathbf{V}_3^k + \beta_4 \mathbf{V}_4^k.$$

2. The next iteration \mathbf{v}^{k+1} is derived from Eq. (6.8) that is solved by the *conjugate gradient* algorithm:

$$\mathbf{v}^{k+1} := (\mathbf{P}_\Theta + \mu \mathbf{I}) \mathbf{v} = \mathbf{f} + \mu \mathbf{V}^k. \quad (6.8)$$

3. Apply the forward qWP transforms to the array \mathbf{v}^{k+1} : $\tilde{\mathbf{F}}_j^\pm \mathbf{v}^{k+1} = \mathbf{C}_j^\pm$, and denote $\tilde{\mathbf{C}}_j^\pm = \mathbf{C}_j^\pm + \mathbf{b}_{\pm j}^k$, where $j = 3, 4$.
4. Select the thresholding parameter λ /(stop the iterations) by the **Select/stop rule** (below).
5. Update the arrays $\mathbf{d}_{\pm j}^k$ by application of the BSA operators $\mathbf{B}_{W_j}^\lambda$, $j = 3, 4$, to the arrays \mathbf{C}_j^\pm

$$\mathbf{d}_{\pm 3}^{k+1} = \mathbf{B}_{W_3}^\lambda \tilde{\mathbf{C}}_3^\pm, \quad \mathbf{d}_{\pm 4}^{k+1} = \mathbf{B}_{W_4}^\lambda \tilde{\mathbf{C}}_4^\pm, \quad \mathbf{d}_j^{k+1} = \mathbf{d}_{+j}^{k+1} \cup \mathbf{d}_{-j}^{k+1}, \quad j = 3, 4.$$

6. Update the arrays $\mathbf{b}_{\pm j}^k$ by $\mathbf{b}_{\pm j}^{k+1} = \mathbf{b}_{\pm j}^k + (\mathbf{C}_j^\pm - \mathbf{d}_{\pm j}^{k+1})$.

7. Go to item 1.

Select/stop rule: The rule is, to some extent, similar to the rule in **Algorithm I** in [22]. Iterations limits are L_1 , L_2 and L_3 . Initial thresholding parameter is $\lambda = \Lambda_1[1]$ and $\nu = 1$. Denote the number of iterations with a certain index ν by K_ν .

- The l_2 norm of the difference $\Delta^{k+1} = \|\mathbf{v}^{k+1} - \mathbf{v}^k\|_2$ is computed,
- If $\nu < R_1$ **and** $\{K_\nu > L_1$ **or** $\Delta^{k+1} < tol_1\}$, then $\nu = \nu + 1$ and $\lambda = \Lambda_1[\nu]$.
- If $R_1 \leq \nu < R_1 + R_2$ **and** $\{K_\nu > L_2$ **or** $\Delta^{k+1} < tol_2\}$, then $\nu = \nu + 1$ and $\lambda = \Lambda_2[\nu - R_1]$.
- If $\nu = R_1 + R_2$ **and** $\{K_\nu > L_3$ **or** $\Delta^{k+1} < tol_2\}$, then **STOP** iterations.
- The array \mathbf{v}^{k+1} is shrunk to the original size $N \times N$ as $\mathbf{v}^{k+1} \succ \tilde{\mathbf{u}}$, and the array $\tilde{\mathbf{u}}$ is taken as a solution to the inpainting problem.

6.2 Experimental results

The performances of our Method1 and Method2 are compared with the performances of the-state-of-the-art inpainting algorithms that use the SET-4 filter banks. The inpainting results by the SET-4 algorithms of the four images from Fig. 5.1, which are degraded by application of four masks displayed in Fig. 6.1 and additive Gaussian noise of various intensities (noise STD $\sigma = 0, 5, 10, 30, 50$ dB), are presented in [6]. The Matlab codes, which produce the results in [6], are available at the web site <http://staffweb1.cityu.edu.hk/xzhuang7/softs/index.html#bdTPCTF>. For each triple *image-mask- σ* , the inpainting results from the application of our Method1 and Method2 are compared with the best result produced by the application of SET-4 algorithms. The results are compared according to PSNR and SSIM values and by visual perception.

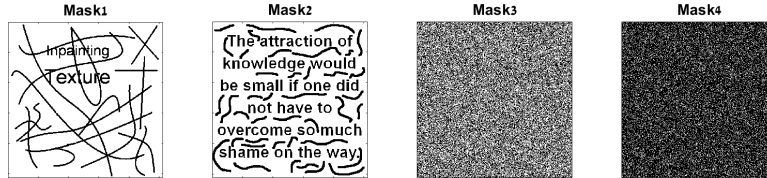


Figure 6.1: Four types of masks: Mask1 – text and thin curves; Mask2 – text and thick curves; Mask3 – 50% of random pixels missing; Mask4 – 80% of random pixels missing

6.2.1 Experiments with “Barbara” image

This image has a complicated structure which comprises smooth regions, multiple edges and oscillating patterns.

1	2	3	4
σ	Method1	Method2	Best out of SET-4
mask1			
0	38.13/0.958	38.33/0.9649	36.68/0.9582 (TP-CTF ₆ [↓])
5	34.93 /0.8256	34.91/ 0.8309	34.05/0.8138 (DAS-2)
10	32.57 /0.7483	32.55/ 0.7526	32.02/0.7393 (DAS-2)
30	28.09 /0.6012	28.01/ 0.6027	27.74/0.5916 (DAS-2)
50	25.85 / 0.5006	25.77/ 0.5035	25.51/0.4894 (DAS-2)
mask2			
0	34.26/0.9222	34.70/0.9321	33.66/0.9234 (DAS-2)
5	32.78 /0.7998	32.75 / 0.8058	32.24/0.7872 (DAS-2)
10	31.13 /0.73	31.11 / 0.7335	30.71/0.7179 (DAS-2)
30	27.22 /0.5791	27.13/ 0.5833	26.95/0.5702 (DAS-2)
50	25.21 /0.4866	25.13/ 0.4873	24.96/0.4709 (DAS-2)
mask3			
0	37.30/0.9005	37.45/0.913	35.72/0.9052 (DAS-2)
5	34.24 /0.7885	34.21/ 0.7932	33.29/0.7784 (DAS-2)
10	31.82/0.7207	31.85/0.7231	31.12/0.7072 (DAS-2)
30	27.1/0.5705	27.17/0.571	26.77/0.5536 (DAS-2)
50	24.84/0.4599	24.9/0.467	24.60/0.4408 (DAS-2)
mask4			
0	30.17/0.7609	30.42/0.7741	29.12/0.7532 (DAS-2)
5	29.28/0.6869	29.44/0.6961	28.41/0.6729 (DAS-2)
10	28.01/0.6256	28.19/0.6331	27.25/0.6088 (DAS-2)
30	24.59 /0.4517	24.45/ 0.4607	24.23/0.4336 (DAS-2)
50	22.67 /0.3474	22.57/ 0.3628	22.35/3254 (DAS-2)

Table 6.1: PSNR/SSIM values for restoration of “Barbara” image. Boldface highlights

Comments on Table 6.1 In all the cases except for one, DAS-2 produces the best result out of SET-4 algorithms. However, all these algorithms were outperformed by Method1 and Method2 in both PSNR and SSIM senses. While in some cases Method1 produces the highest PSNR values, the SSIM values for Method2 significantly exceed these for Method1 and, especially, for DAS-2. Figures 6.2, 6.3 and 6.4 illustrate the restoration of “Barbara”, which was severely degraded by the application of mask2 and strong additive Gaussian noise with $\sigma = 50$ dB, by Method2 and DAS-2. Figure 6.2 shows that both algorithms successfully inpainted the mask and suppressed the noise but, in doing so, DAS-2 loses thin texture details and adds some artifacts into the image. Figure 6.4 demonstrates this.

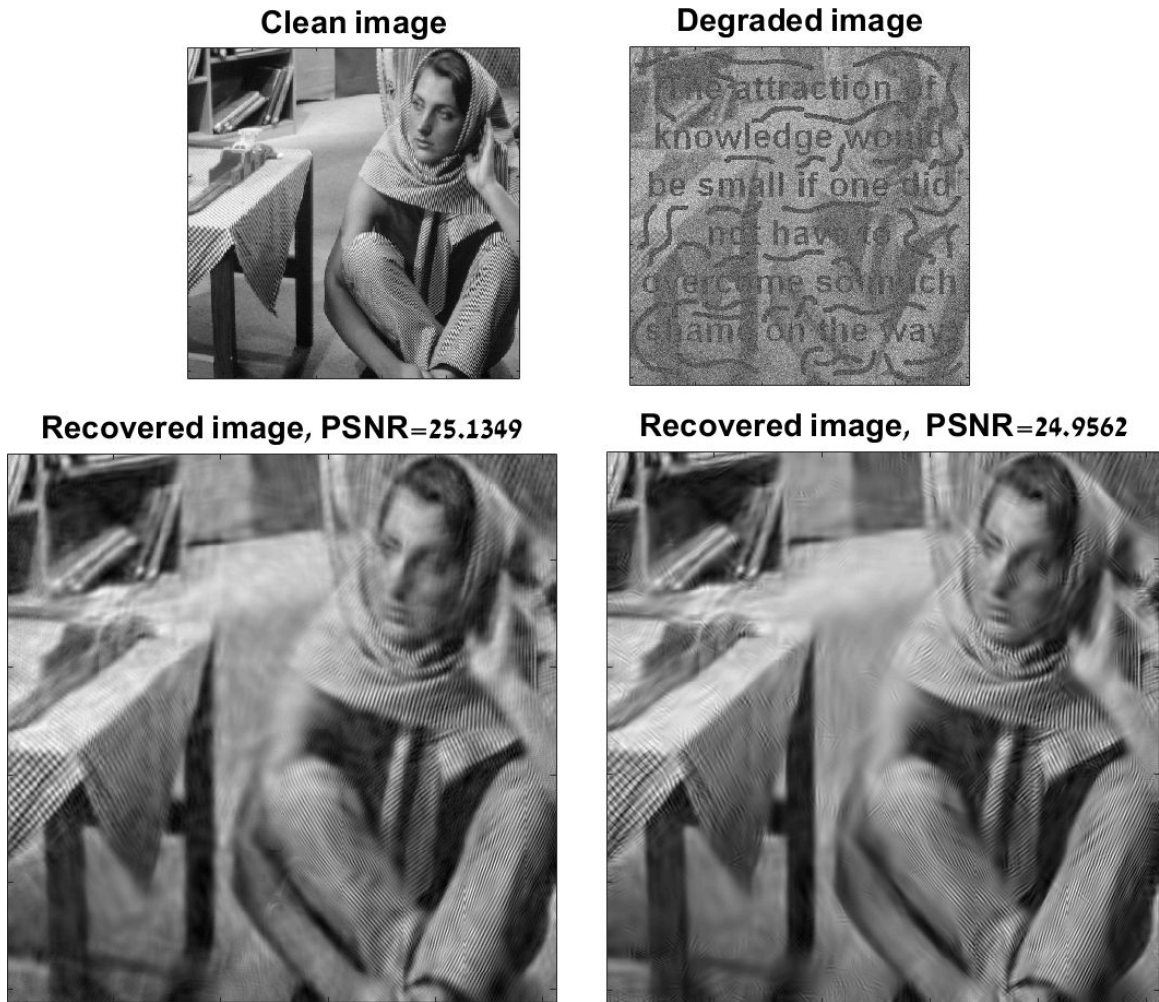


Figure 6.2: Restoration of “Barbara” image. Top left: clean image. Top right: image degraded by application of mask2 and additive Gaussian noise with $\sigma = 50$ dB. Bottom left: Restoration by method2, PSNR=25.13 dB, SSIM=0.4873. Bottom right: Restoration by DAS-2, PSNR=24.96 dB, SSIM=0.4709

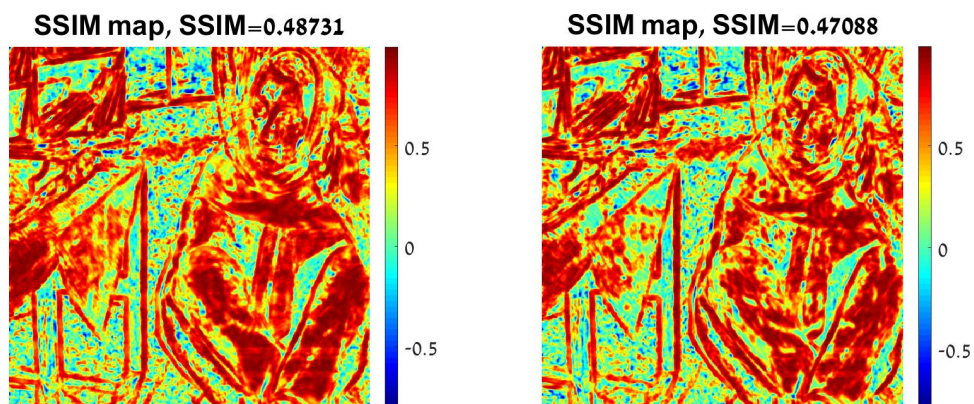


Figure 6.3: SSIM map of images restored by Method2 (left) and DAS-2 (right)

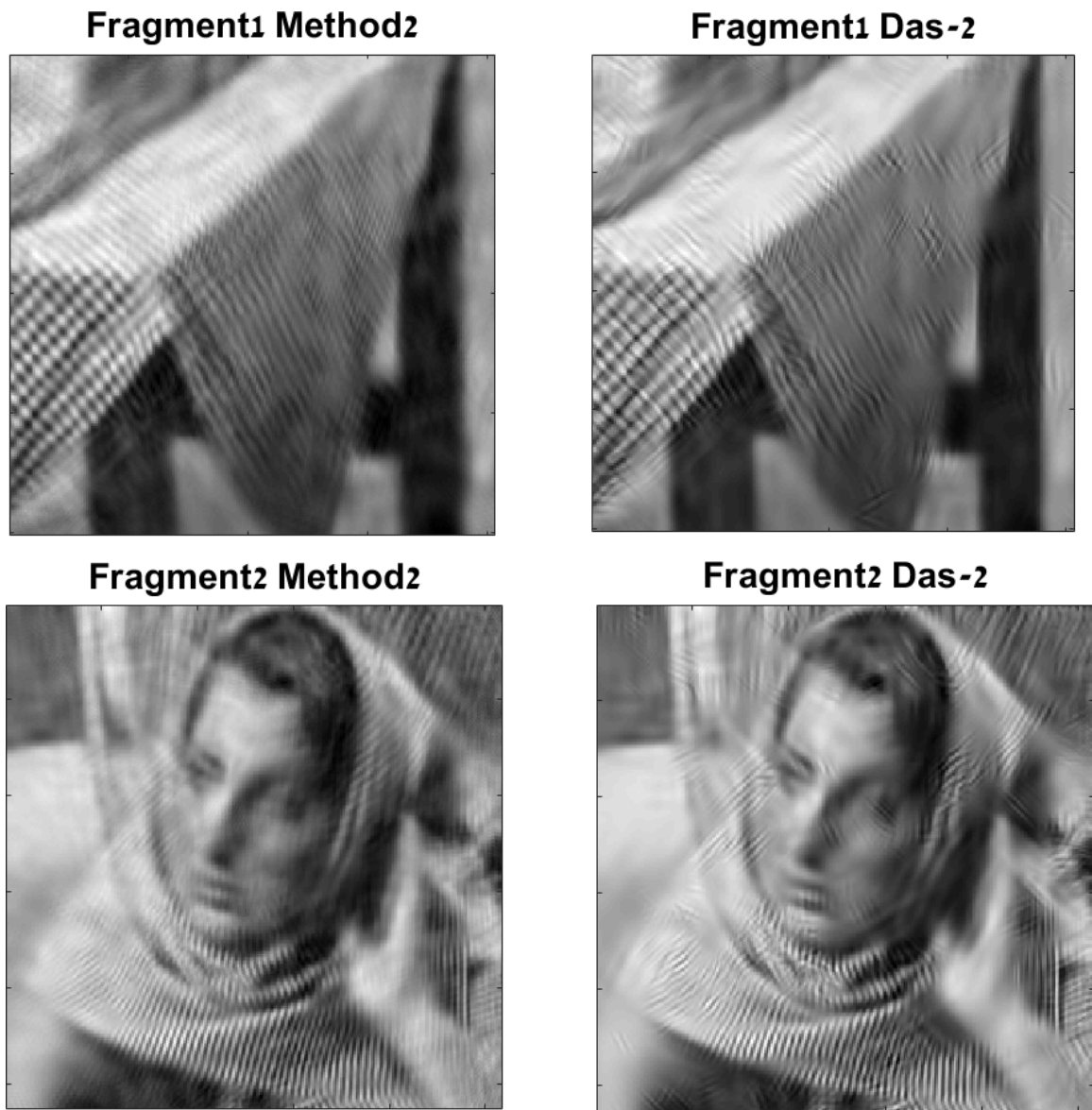


Figure 6.4: Fragments of images displayed in Fig. 6.2

6.2.2 Experiments with “Fingerprint” image

This image consists of oscillatory patterns in various directions.

.. 1	2	3	4
σ	Method1	Method2	Best out of SET-4
mask1			
0	31.93/0.9778	32.64/0.9804	31.72/0.9755 (TP-CTF ₆ [↓])
5	30.69/0.9633	30.86/0.9644	30.36/0.9596 (DAS-2)
10	28.96/0.9386	29.09/0.9404	28.77/0.9352 (DAS-2)
30	25.15/0.8426	25.22/0.8479	25.04/0.8389 (DAS-2)
50	23.26/0.7674	23.42/0.7781	23.21/0.7656 (DAS-2)
mask2			
0	28.76/0.9488	28.94/0.9503	28.31/0.9416 (TP-CTF ₆ [↓])
5	28.02/0.9376	28.1/0.9347	27.68/0.9261 (DAS-2)
10	27.01/0.9081	27.08/0.9114	26.76/0.9026 (DAS-2)
30	24.16/0.8123	24.35/0.8224	24.15/0.8091 (DAS-2)
50	22.58/0.739	22.77/0.7528	22.65/0.738 (DAS-2)
mask3			
0	34.53/0.9785	34.54/0.9786	34.19/0.977 (TP-CTF ₆ [↓])
5	31.72/0.9583	31.84/0.9598	31.54/0.9572 (TP-CTF ₆ [↓])
10	29.14/0.9260	29.37/0.9315	29.09/0.9267 (TP-CTF ₆ [↓])
30	24.51/0.8088	24.73/0.8254	24.43/0.8055 (TP-CTF ₆ [↓])
50	22.48/0.7211	22.69/0.7478	22.53/0.7217 (DAS-2)
mask4			
0	27.03/0.8989	26.83/0.8959	26.77/0.8936 (TP-CTF ₆ [↓])
5	26.27/0.8778	26.14/0.8771	25.87/0.8715 (TP-CTF ₆ [↓])
10	25.11/0.8428	25.11/0.8452	24.60/0.8341 (TP-CTF ₆ [↓])
30	22.09/0.7124	22.15/0.7308	22.11/0.7115 (DAS-2)
50	20.32/0.6126	20.49/ 0.6417	20.60/0.6114 (DAS-2)

Table 6.2: PSNR/SSIM values for restoration of “Fingerprint” image. Boldface highlights the best results. σ – noise STD

Comments on Table 6.2 For the “Fingerprint” image, in most experiments DAS-2 produces the best result from SET-4 algorithms, while for the rest TP-CTF₆[↓] is the best. However, all these algorithms were outperformed by Method1 and Method2 in both PSNR and SSIM senses. While in three cases Method1 produces the highest PSNR and SSIM values, in the rest of the cases, Method2 significantly outperforms Method1 and, especially, the SET-4 algorithms. Note that all the SSIM values that were produced by Method1 were higher than those produced by SET-4 algorithms. Figures 6.5, 6.6 and 6.7 illustrate the restoration of the “Fingerprint” image, which was severely degraded by the application of mask4 (80% of the pixels missing) and strong additive Gaussian noise with $\sigma = 50$ dB, by Method2 and DAS-2. In this single case, the PSNR for restoration by DAS-2 is a little bit higher than the restoration by Method2, which is not the case for the SSIM. Figure 6.5 shows that both algorithms successfully inpainted the mask and suppressed the noise but, in doing so, DAS-2 over smoothed some parts of the image. It is seen in Fig. 6.7.

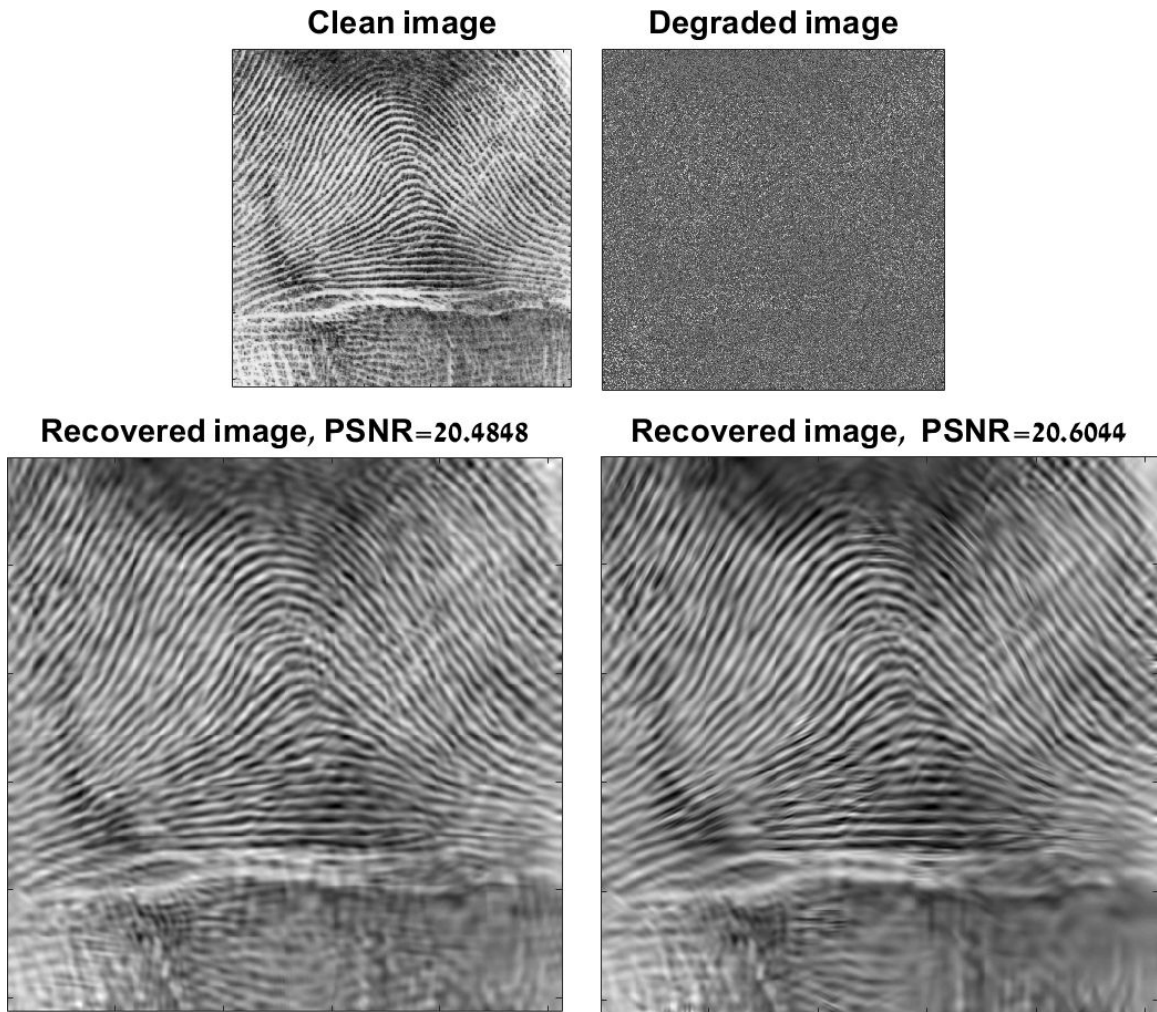


Figure 6.5: Restoration of “Fingerprint” image. Top left: clean image. Top right: image degraded by the application of mask4 and additive Gaussian noise with $\sigma = 50$ dB. Bottom left: Restoration by Method2, PSNR=20.48 dB, SSIM=0.6417. Bottom right: Restoration by DAS-2, PSNR=20.6 dB, SSIM=0.6138

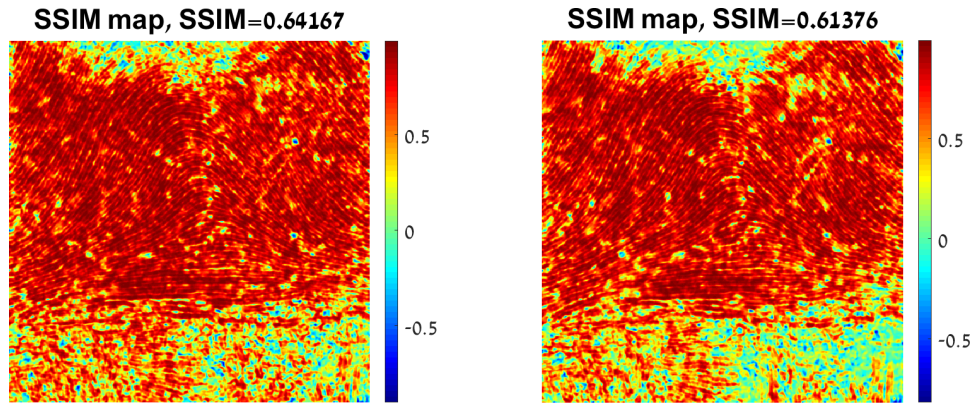


Figure 6.6: SSIM map of images restored by Method2 (left) and DAS-2 (right)

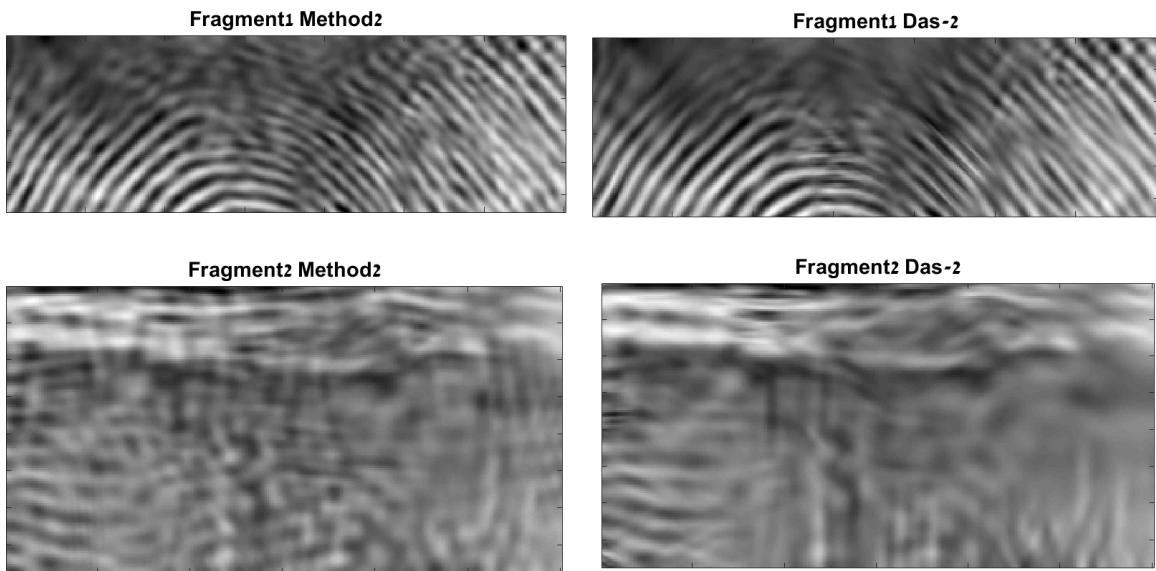


Figure 6.7: Fragments of images displayed in Fig. 6.5

6.2.3 Experiments with “Lena” image

This image is characterized by a number of edges separating smooth areas and some fine details such as hair and the hat decoration.

1	2	3	4
σ	Method1	Method2	Best out of SET-4
mask1			
0	37.50/0.9371	37.75/0.9474	38.02/0.9487 (TP-CTF ₆)
5	34.94/0.7017	34.95/ 0.7241	35.19 /0.6717 (TP-CTF ₆)
10	33.18/0.605	33.22/ 0.6138	33.42 /0.5857 (TP-CTF ₆)
30	29.34/0.4490	29.43/ 0.4542	29.81 /0.4494 (TP-CTF ₆)
50	27.31/0.3704	27.40/ 0.3774	27.85 /0.377 (TP-CTF ₆)
mask2			
0	33.72/0.884	33.96/0.8988	34.3/0.90 (TP-CTF ₆)
5	32.48/0.661	32.43/ 0.692	32.97 /0.6466 (TP-CTF ₆)
10	31.39/0.5815	31.37/ 0.5934	31.78 /0.5667 (TP-CTF ₆)
30	28.39/0.4319	28.51/ 0.4398	28.89 /0.434 (TP-CTF ₆)
50	26.68/0.3557	26.65/ 0.3637	27.22 /0.3620 (TP-CTF ₆)
mask3			
0	37.70/0.813	37.68/0.8456	38.0/0.8520 (TP-CTF ₆)
5	35.14/0.6465	35.17/ 0.6599	35.40 /0.6316 (TP-CTF ₆)
10	33.03/0.5682	33.04/ 0.5771	33.40 /0.5575 (TP-CTF ₆)
30	28.67/0.4183	28.81/ 0.4246	29.18 /0.4205 (TP-CTF ₆)
50	26.51/0.3409	26.57/ 0.3476	27.06 /0.3461 (TP-CTF ₆)
mask4			
0	32.09/0.6311	31.93/0.6648	32.33/0.6741 (TP-CTF ₆)
5	31.18/0.5519	31.15/ 0.5531	31.44 /0.5505 (TP-CTF ₆)
10	29.86/0.4843	29.89/0.4851	30.25/0.4872 (TP-CTF ₆)
30	26.40/0.3406	26.51/0.3480	26.95/0.3481 (TP-CTF ₆)
50	24.25/0.2595	24.52/0.2741	25.15/0.2753 (TP-CTF ₆)

Table 6.3: PSNR/SSIM values for restoration of “Lena” image. Boldface highlights the best results. σ – noise STD

Comments on Table 6.3 For the “Lena” image, TP-CTF₆ produces the best results from the SET-4 algorithms and the PSNR of the restored images is higher than the PSNR that is produced by Method1 and Method2. However, in most cases, the highest SSIM values are achieved by Method2. This is an indication to the fact that generally Method2 restores the image structure better than TP-CTF₆. It is illustrated in Figs. 6.8, 6.9 and 6.10. These figures display the restoration results of the “Lena” image, which was severely degraded by the application of mask3 (50% of pixels are missing) and strong additive Gaussian noise with $\sigma = 50$ dB, by Method2 and TP-CTF₆. Although the PSNR of the restoration by TP-CTF₆ is higher than that for Method2 and the SSIM values were close to each other, fine details, which were lost by TP-CTF₆, are retained by Method2. It is seen in Fig. 6.10.

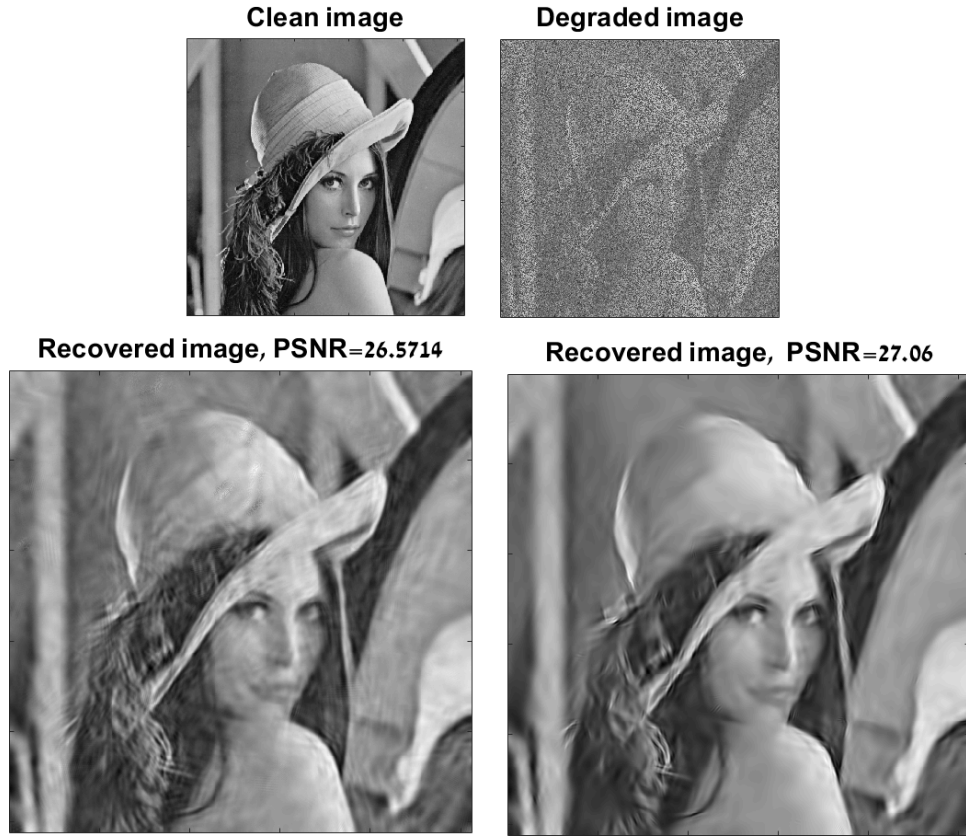


Figure 6.8: Restoration of “Lena” image. Top left: clean image. Top right: image degraded by application of mask3 and additive Gaussian noise with $\sigma = 50$ dB. Bottom left: Method2 restoration, PSNR=26.57 dB, SSIM=0.3476. Bottom right: TP-CTF₆ restoration, PSNR=27.06 dB, SSIM=0.3461

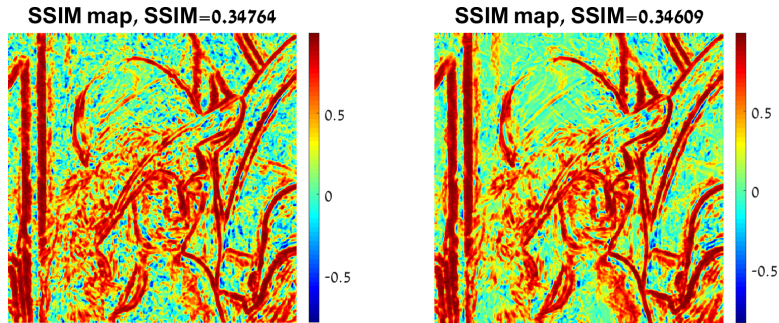


Figure 6.9: SSIM map of images restored by Method2 (left) and TP-CTF₆ (right)

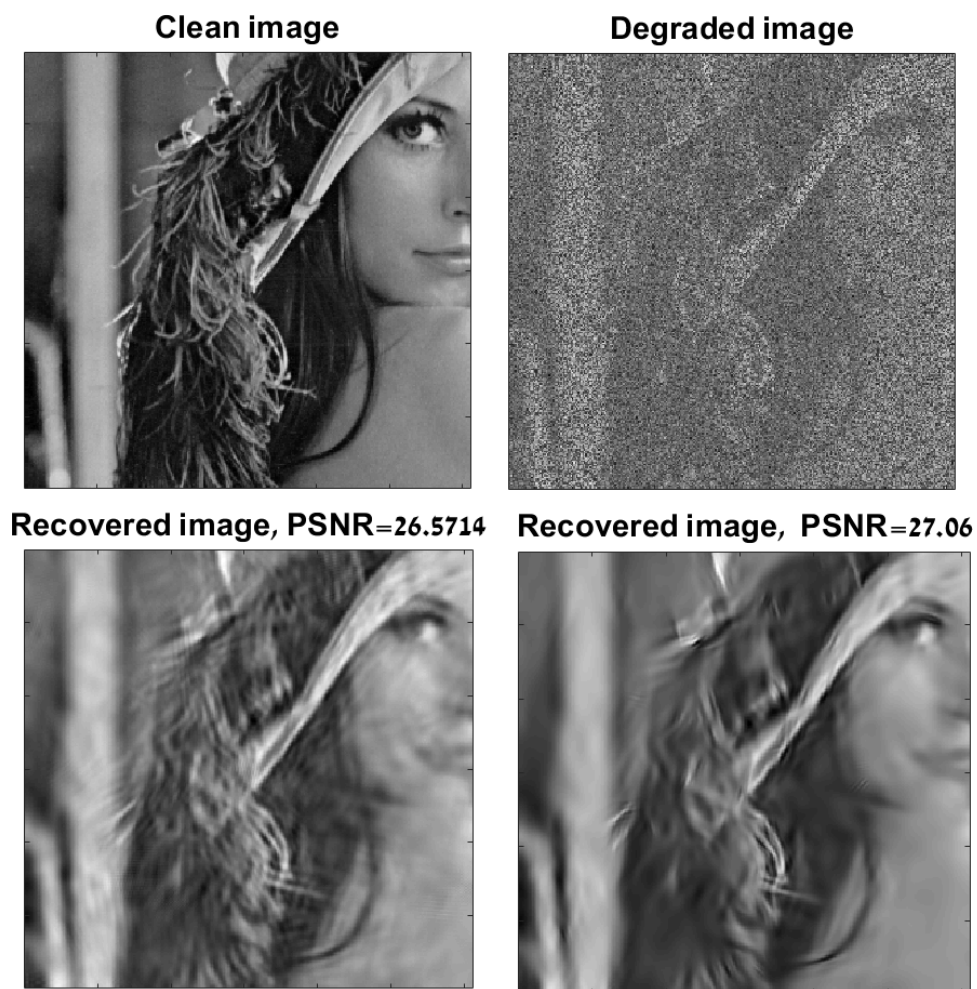


Figure 6.10: Fragments of images displayed in Fig. 6.8

6.2.4 Experiments with “Boat” image

This image is characterized by multiple sharp edges separating smooth areas (the sky) and texture (the ground).

1	2	3	4
σ	Method1	Method2	Best out of SET-4
mask1			
0	34.78/0.9363	34.76/0.9389	34.96/0.9407 (TP-CTF ₆)
5	32.68/0.7783	32.68/ 0.7924	32.81 /0.7521 (TP-CTF ₆)
10	30.79/0.6594	30.75/ 0.674	31.04 /0.6301 (TP-CTF ₆)
30	27.03/0.4538	27.02/ 0.4626	27.41 /0.4334 (TP-CTF ₆)
50	25.22/0.3479	25.15/ 0.3604	25.6 /0.3342 (DAS-1)
mask2			
0	30.23/0.8739	30.44/0.8783	30.80/0.8813 (TP-CTF ₆)
5	29.30/0.7211	29.29/ 0.7411	29.79 /0.7183 (DAS-2)
10	28.18/0.6114	28.25/ 0.6304	28.85 /0.59 (DAS-1)
30	25.78/0.4167	25.83/ 0.4303	26.34 /0.4069 (DAS-1)
50	24.33/0.3193	24.37/ 0.3336	24.84 /0.3123 (DAS-1)
mask3			
0	34.39/0.8518	34.43/0.8624	34.42/0.8581 (TP-CTF ₆)
5	32.26/0.7002	32.11/ 0.7235	32.50 /0.6835 (TP-CTF ₆)
10	30.3/0.5978	30.19/ 0.6166	30.65 /0.5864 (TP-CTF ₆)
30	26.33/0.4045	26.45/ 0.4265	26.66 /0.3802 (TP-CTF ₆)
50	24.43/0.2993	24.438/ 0.3293	24.75 /0.2783 (TP-CTF ₆)
mask4			
0	28.39/0.6288	28.16/0.6396	28.58/0.6428 (TP-CTF ₆)
5	27.7/0.5435	27.71/ 0.5576	27.98 /0.5461 (TP-CTF ₆)
10	26.77/0.4652	26.73/ 0.48	27.08 /0.4648 (TP-CTF ₆)
30	24.01/0.2775	24.0/ 0.308	24.46 /0.2770 (TP-CTF ₆)
50	22.50/0.1961	22.22/ 0.2327	22.96 /0.1926 (TP-CTF ₆)

Table 6.4: PSNR/SSIM values for restoration of “Boat” image. Boldface highlights the best results. σ – noise STD

Comments on Table 6.4 In all the cases for the “Boat” image except for one, the PSNR of images restored by one of the SET-4 algorithms (TP-CTF₆, DAS-1 and DAS-2) is higher than the PSNR produced by Method1 and Method2. However, in almost all cases, the SSIM values produced by Method2 significantly exceed the values produced by the SET-4 algorithms. In most cases, the Method1 SSIM values also are higher than those produced by the SET-4 algorithms. This is an indication to the fact that generally Method2 (and in many cases, Method1) restores the image structure better than any of the SET-4 algorithms. It is illustrated in Figs. 6.11, 6.12 and 6.13. These figures display the results of the “Boat” restoration, which was severely degraded by the application of mask3 (50% of pixels are missing) and strong additive Gaussian noise with $\sigma = 50$ dB, by Method2 and TP-CTF₆. Although the PSNR for restoration by TP-CTF₆ is higher than that by Method2, the Method2-SSIM value is much higher than that produced by TP-CTF₆. The restored image by TP-CTF₆ looks strongly over-smoothed compared to the image restored by Method2. Some edges and almost the entire texture in the image were lost by the application of TP-CTF₆ but were retained by Method2. It is seen in Fig. 6.13.

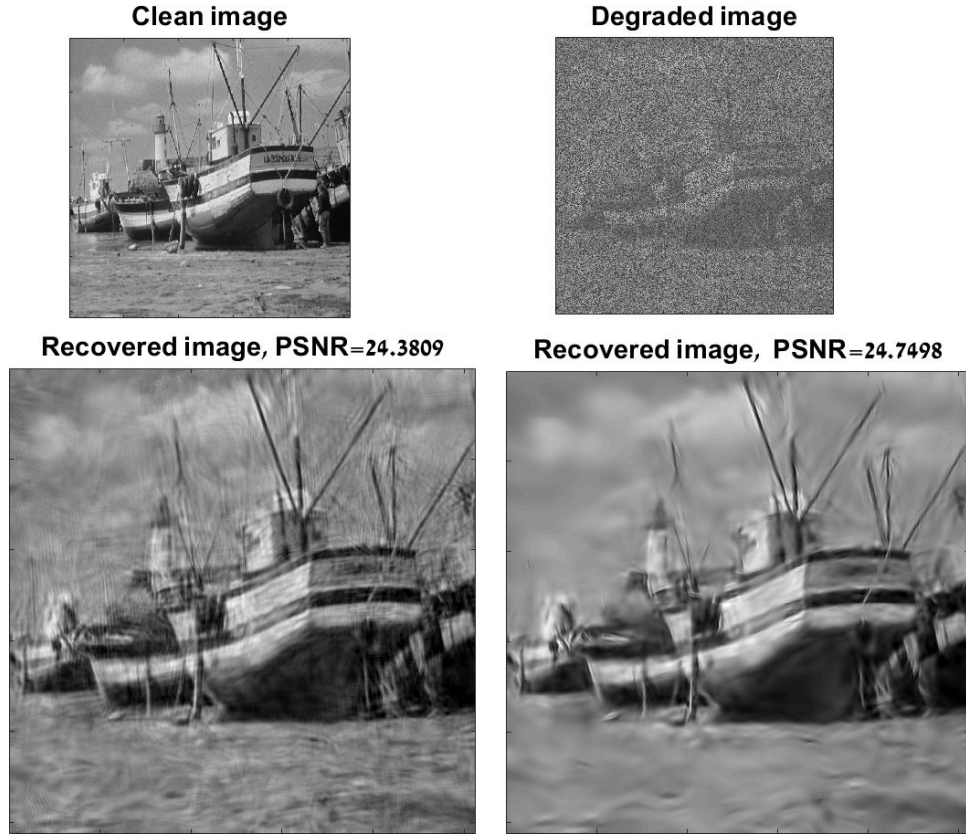


Figure 6.11: Restoration of “Boat” image. Top left: clean image. Top right: image degraded by the application of mask3 and additive Gaussian noise with $\sigma = 50$ dB. Bottom left: Restoration by Method2, PSNR=24.38 dB, SSIM=0.3293. Bottom right: Restoration by TP-CTF₆, PSNR=24.75 dB, SSIM=0.2783

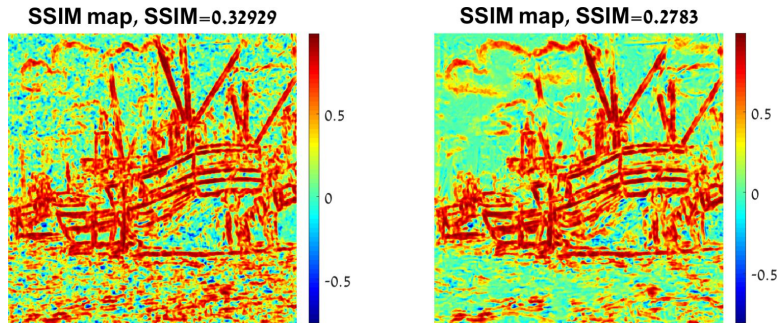


Figure 6.12: SSIM map of images restored by Method2 (left) and TP-CTF₆ (right)

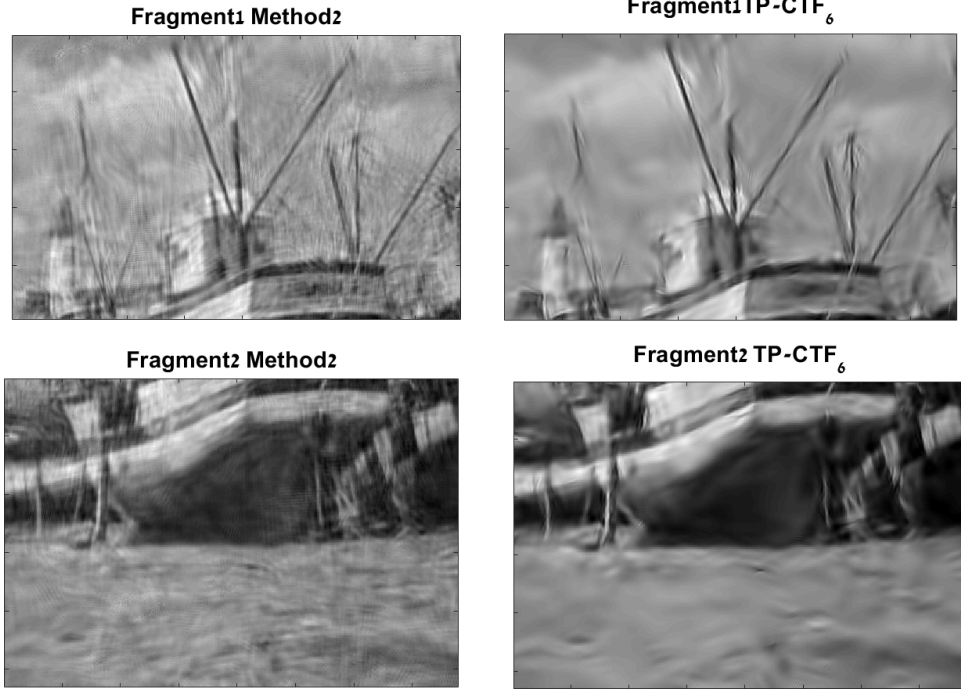


Figure 6.13: Fragments of images displayed in Fig. 6.11

7 Discussion

The quasi-analytic directional discrete-time wavelet packets (qWPs) designed in [1] were applied to denoising and inpainting. The qWPs operate in two-dimensional spaces of periodic signals. Seemingly, the requirement of periodicity imposes some limitations on the scope of signals available for processing, but actually these limitations are easily circumvented by symmetrical extension of images beyond the boundaries before processing and shrinkage to the original size after that. On the other hand, the periodic setting provides a lot of substantial opportunities for the design and implementation of WP transforms.

Denoising: Our general approach to handle the denoising problem is, to some extent, conventional: we decompose the corrupted image $\tilde{\mathbf{X}}$ into two sets $\{\tilde{\mathbf{Z}}_{+[m]}^{j,l}\}$ and $\{\tilde{\mathbf{Z}}_{-[m]}^{j,l}\}$, $m = 1, \dots, M$, $j, l = 0, 2^m - 1$, of the qWP transform coefficients, implement the Bivariate Shrinkage algorithm (BSA)[21, 7] to the transform coefficients, and restore the image $\tilde{\mathbf{X}} \approx \mathbf{X}$ from the shrunk coefficients from several decomposition levels.

The experiments demonstrate that the above scheme, which uses the designed qWP transforms, produces results competitive with the best existing denoising methods such as the *Block-matching and 3D filtering (BM3D)* ([8], *Directional Compactly Supported Tensor Product Complex Tight Framelets (cptTP-CTF₆)* ([26]) and *Digital Affine Shear Filter Transform with 2-Layer Structure (DAS-2)* ([6]). In particular, the qWP algorithm proved to be highly efficient in restoring edges, fine texture details and oscillatory patterns even from severely degraded images with complicated structure such as “Barbara” and “Fingerprint”. This ability stems from valuable properties of the qWP transforms, such as:

- The qWP transforms provide a variety of 2D waveforms oriented in multiple directions. For example, fourth-level qWPs are oriented in 62 different directions.
- These waveforms possess symmetry properties and are close to directional cosines with a variety of frequencies modulated by spatially localized low-frequency 2D signals.
- The DFT spectra of the waveforms produce a refined split of the frequency domain.
- Fast implementation of the transforms by using the FFT enables us to use the transforms with increased redundancy. For example, implementation of the algorithm’s version involves WPs from three decomposition levels (redundancy rate $RR=6$) takes 1.2 seconds, while the two-level version ($RR=4$) takes 0.8 and the fast one-level version ($RR=2$) takes only 0.4 second. Such a rapidity (which can be significantly increased by code optimization, parallelization and compiling .MEX files) together with the automatic evaluation of the noise level inherent to the qWP algorithm makes it possible to use the algorithm for video denoising.

Inpainting: The above listed properties of qWP transforms are proved to be indispensable while dealing with inpainting problem. We presented two qWP-based methods for image inpainting: Method1 (**M1**) is a slight modification of inpainting **Algorithm I** introduced in [22, 23]. **Algorithm I** uses TP-CTF₆ that produces excellent image inpainting results that outperform (in a PSNR sense) most state-of-the-art methods (see [22] for methods comparison). In [6], **Algorithm I** is implemented using SET-4 filter banks. Method1 consists of iterative thresholding of transform coefficients with decreasing localized thresholds whose levels are determined automatically by using the BSA. Method2 (**M2**) is a coupling of **M1** with the Split Bregman Iterations (SBI) scheme. In essence, it is the SBI algorithm supplied with decreasing localized thresholds that is determined by BSA.

In multiple experiments, the performance of our **M1** and **M2** is compared with the performance of the-state-of-the-art inpainting algorithms that use SET-4 filter banks. The inpainting results by the latter algorithms for four images in Fig. 5.1, which are degraded by application of four masks displayed in Fig. 6.1 and additive Gaussian noise of various intensities (noise STD $\sigma = 0, 5, 10, 30, 50$ dB), are presented in [6]. For each triple *image-mask- σ* , the inpainting results (**M1** and **M2** vs. SET-4 algorithms) are compared through PSNR and SSIM values and by visual perception. In all the experiments, our methods succeeded in inpainting of even severely degraded images and in suppressing noise. In most cases, thin structures were recovered. On images with complicated structure such as “Barbara” and “Fingerprint”, **M1** and especially **M2**, significantly outperform SET-4 algorithms in all three (PSNR, SSIM and perception) senses. As for “Lena” and “Boat” images, while in most experiments SET-4 algorithms produce higher PSNR values compared to **M1** and **M2**, the SSIM values are higher for **M1** and especially for **M2**. This fact indicates that our **M1** and **M2** are superior over SET-4 algorithms in the image structure recovery. Visual observations confirm this claim that is illustrated in Figs. 6.8–6.13.

Generally, we claim that our **M1** and especially **M2**, which are based on directional quasi-analytic wavelet packets originated from discrete splines, are powerful tools for images restoration that are severely degraded by loss of the majority of the pixels and have strong additive noise. The methods succeed in capturing the fine details in the images in cases where other state-of-the-art algorithms fail to do it. This fact is illustrated in FIG. 7.1, which displays the restoration results of the ‘Mandrill’ image from the input where 80% of pixels are missing and

additive Gaussian noise with $\sigma = 50$ dB is present. While the output from DAS-2 algorithm (which was the best out of SET-4 for this image) has PSNR=19.81 dB compared to 19.37 dB produced by **M2**, the SSIM for the **M2** restoration is 0.2185 compared to 0.1414 for DAS-2. Figure 7.2 displays the SSIM maps for **M2** and DAS-2, which significantly differ from each other.

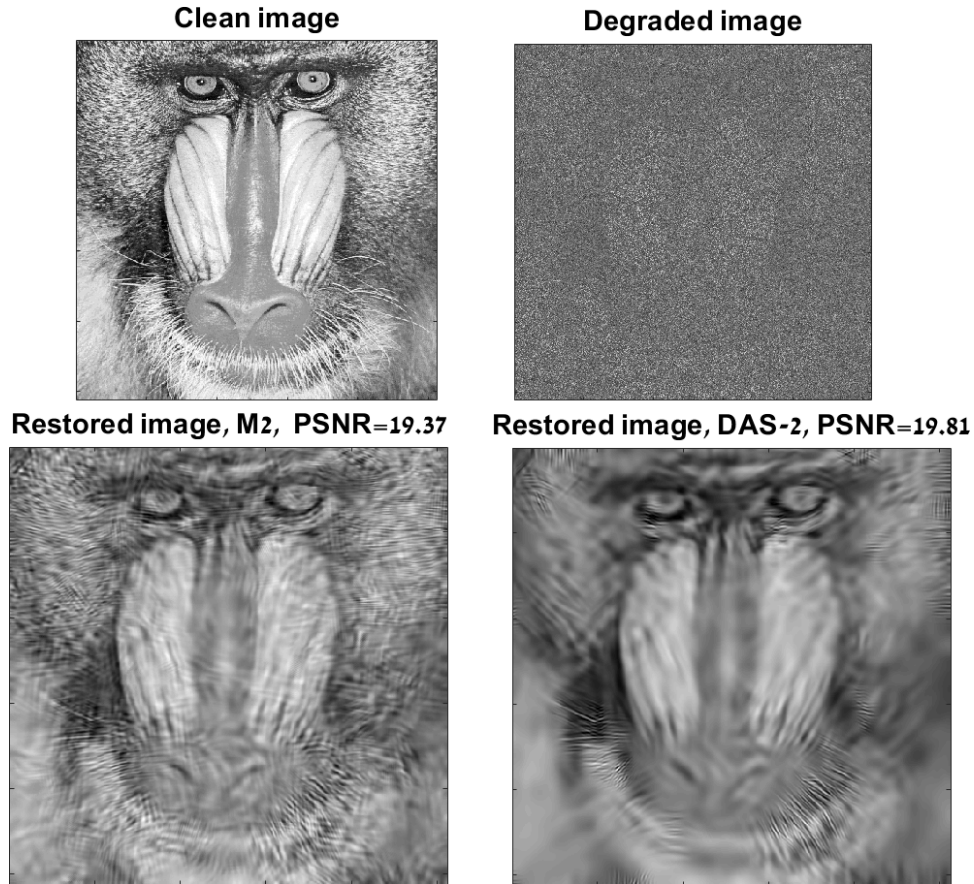


Figure 7.1: Restoration of “Mandrill” image. Top left: clean image. Top right: image degraded by application of mask4 with additive Gaussian noise with $\sigma = 50$ dB. Bottom left: Method2 restoration, PSNR=19.37 dB, SSIM=0.2185. Bottom right: DAS-2 restoration, PSNR=19.81 dB, SSIM=0.1414

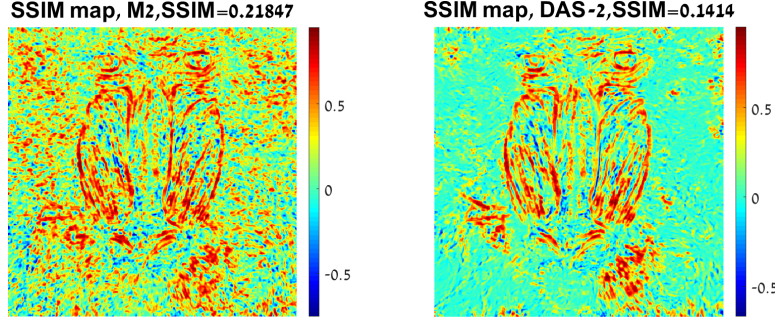


Figure 7.2: SSIM map of images restored by Method2 (left) and DAS-2 (right)

Figures 7.1 and 7.2 are good illustrations to the fact that the SSIM is much more informative characteristics than the PSNR.

Summarizing, having such a versatile and flexible tool at hand, multiple data processing problems such as image deblurring, superresolution, segmentation and classification, target detection (here the directionality is of utmost importance), extraction of characteristic features in signals and images can be addressed. The 3D directional wavelet packets, whose designing is underway, may be beneficial for seismic and hyper-spectral processing.

Acknowledgment This research was partially supported by the Israel Science Foundation (ISF, 1556/17), Blavatnik Computer Science Research Fund Israel Ministry of Science and Technology 3-13601.

References

- [1] A. Averbuch, P. Neittaanmäki, and V. Zheludev. Analytic and directional wavelet packets in the space of periodic signals. <https://arXiv.org/abs/1907.01479>.
- [2] A. Averbuch, P. Neittaanmäki, and V. Zheludev. Periodic spline-based frames: Design and applications for image restoration. *Inverse Problems and Imaging*, 9(3):661–707, 2015.
- [3] A. Averbuch, P. Neittaanmäki, and V. Zheludev. *Splines and spline wavelet methods with application to signal and image processing, Volume III: Selected topics*. Springer, 2019.
- [4] A. Z. Averbuch, P. Neittaanmäki, and V. A. Zheludev. *Spline and spline wavelet methods with applications to signal and image processing, Volume I: Periodic splines*. Springer, 2014.
- [5] I. Bayram and I. W. Selesnick. On the dual-tree complex wavelet packet and m-band transforms. *IEEE Trans. Signal Process.*, 56:2298–2310, 2008.
- [6] Z. Che and X. Zhuang. Digital affine shear filter banks with 2-layer structure and their applications in image processing. *IEEE Transactions on Image Processing*, 27(8):3931–3941, 2018.
- [7] L. Şendur and I. W. Selesnick. Bivariate shrinkage functions for wavelet-based denoising exploiting interscale dependency. *IEEE Trans. Signal Process.*, 50:2744–2756, 2002.

- [8] K. Dabov, A. Foi, V. Katkovnik, and K. Egiazarian. Image denoising by sparse 3d transform-domain collaborative filtering. *IEEE Trans. Image Process.*, 16(8):2080–2095, 2007.
- [9] T. Goldstein and S. Osher. The split Bregman method for L_1 -regularized problems. *SIAM J. Imaging Sci.*, 2(2):323–343, 2009.
- [10] B. Han and Z. Zhao. Tensor product complex tight framelets with increasing directionality. *SIAM J. Imaging Sci.*, 7(2):997–1034, 2014.
- [11] B. Han, Z. Zhao, and X. Zhuang. Directional tensor product complex tight framelets with low redundancy. *Appl. Comput. Harmon. Anal.*, 41(2):603–637, 2016.
- [12] B. Han and X. Zhuang. Smooth affine shear tight frames with *MRA* structures. *Appl. Comput. Harmon. Anal.*, 39(2):300–338, 2015.
- [13] A. Jalobeanu, L. Blanc-Féraud, and J. Zerubia. Satellite image deconvolution using complex wavelet packets. In *Proc. IEEE Int. Conf. Image Process. (ICIP)*, pages 809–812, 2000.
- [14] A. Jalobeanu, L. Blanc-Féraud, and J. Zerubia. Satellite image deblurring using complex wavelet packets. *Int. J. Comput. Vision*, 51(3):205–217, 2003.
- [15] A. Jalobeanu, N. Kingsbury, and J. Zerubia. Image deconvolution using hidden markov tree modeling of complex wavelet packets. In *Proc. IEEE Int. Conf. Image Process. (ICIP)*, pages 201–204, 2001.
- [16] H. Ji, Z. Shen, and Y. Xu. Wavelet based restoration of images with missing or damaged pixels. *East Asian J. Appl. Math.*, 1(2):108–131, 2011.
- [17] N.G. Kingsbury. Image processing with complex wavelets. *Philos. Trans. R. Soc. London A, Math. Phys. Sci.*, 357(1760):2543–2560, 1999.
- [18] N.G. Kingsbury. Complex wavelets for shift invariant analysis and filtering of signals. *J. Appl. Comput. Harm. Anal.*, 10(3):234–253, 2001.
- [19] A. V. Oppenheim and R. W. Schaffer. *Discrete-time signal processing*. Prentice Hall, New York, 3rd edition, 2010.
- [20] I.W. Selesnick, R.G. Baraniuk, and N.G. Kingsbury. The dual-tree complex wavelet transform. *IEEE Signal Process. Mag.*, 22(6):123–151, 2005.
- [21] L. Şendur and I. Selesnick. Bivariate shrinkage with local variance estimation. *IEEE Signal Process. Letters*, 9(12):438–441, 2002.
- [22] Y. Shen, B. Han, and E. Braverman. Image inpainting using directional complex tight framelets. *Preprint, arXiv: 1407.3234*, 2014.
- [23] Y. Shen, B. Han, and E. Braverman. Image inpainting from partial noisy data by directional complex tight framelets. *Anziam J.*, 58(3–4):1–9, 2017.
- [24] Z. Wang, A. C. Bovik, H. R. Sheikh, and E. P. Simoncelli. Image quality assessment: From error visibility to structural similarity. *IEEE Trans. Image Proc.*, 13(4):600–612, 2004.

- [25] Z. Xie, E.Wang, G. Zhang, G. Zhao, and X. Chen. Seismic signal analysis based on the dual-tree complex wavelet packet transform. *Acta Seismologica Sinica*, 17(1):117–122, 2004.
- [26] H. Zhuang and B. Han. Compactly supported tensor product complex tight framelets with directionality. In *2019 International Conference on Sampling Theory and Applications (SampTA), Bordeaux, France*.
- [27] X. Zhuang. Digital affine shear transforms: fast realization and applications in image/video processing. *SIAM J. Imag. Sci.*, 9(3):1437–1466, 2016.